Fermi National Accelerator Laboratory

FERMILAB-Pub-94/346-E

Measurement of the Branching Ratio and Asymmetry Parameter for the $\Sigma^+ \rightarrow p\gamma$ Radiative Delay

S. Timm et. al
The E761 Collaboration

Fermi National Accelerator Laboratory, P.O. Box 500, Batavia, Illinois 60510
Petersburg Nuclear Physics Institute, Gatchina, Russia
Institute of High Energy Physics, Beijing, PRC
H.H. Wills Physics Laboratory, University of Bristol, UK
Carnegie Mellon University, Pittsburgh, PA 15213
Institute of Theoretical and Experimental Physics, Moscow, Russia
State University of New York at Albany, Albany NY 12222
Universidade Federal da Paraiba, Paraiba, Brazil
Centro Brasileiro de Pesquisas Fisicas, Rio De Janeiro, Brazil
Conselho Nacional de Pesquisas CNPq, Rio de Janeiro, Brazil
Universidade de Sao Paulo, Sao Paulo, Brazil
J.W. Gibbs Laboratory, Yale University, New Haven CT 06511

October 1994

Submitted to *Physical Review D*

Operated by Universities Research Association Inc. under Contract No. DE-AC02-76CHO3000 with the United States Department of Energy

Disclaimer

This report was prepared as an account of work sponsored by an agency of the United States Government. Neither the United States Government nor any agency thereof, nor any of their employees, makes any warranty, express or implied, or assumes any legal liability or responsibility for the accuracy, completeness, or usefulness of any information, apparatus, product, or process disclosed, or represents that its use would not infringe privately owned rights. Reference herein to any specific commercial product, process, or service by trade name, trademark, manufacturer, or otherwise, does not necessarily constitute or imply its endorsement, recommendation, or favoring by the United States Government or any agency thereof. The views and opinions of authors expressed herein do not necessarily state or reflect those of the United States Government or any agency thereof.

Measurement of the Branching Ratio and Asymmetry Parameter for the $\Sigma^+ \rightarrow p\gamma$ Radiative Decay.

S. Timm(5), I. F. Albuquerque(12), N. F. Bondar(2), R. Carrigan Jr.(1), D. Chen(8),*, P. S. Cooper(1), Dai Lisheng(3), A. S. Denisov(2), A. V. Dobrovolsky(2), T. Dubbs(6),†, A. M. F. Endler(10), C. O. Escobar(12), M. Foucher(13),‡, V. L. Golovtsov(2), H. Gottschalk(1),§, P. Gouffon(12), V. T. Grachev(2), A. V. Khanzadeev(2), M. A. Kubantsev(7), N. P. Kuropatkin(2), J. Lach(1), Lang Pengfei(3), J. Langland(6), Li Chengze(3), Li Yunshan(3), M. Luksys(9), J. R. P. Mahon(12),**, E. McCliment(6), A. Morelos(1),††, C. Newsom(6), M. C. Pommot Maia(11),‡‡, V. M. Samsonov(2), V. A. Schegelsky(2), Shi Huanzhang(3), V. J. Smith(4), Tang Fukun(3), N. K. Terentyev(2), I. I. Tkatch(2), L. N. Uvarov(2), A. A. Vorobyov(2), Yan Jie(3), Zhao Wenheng(3), Zheng Shuchen(3), Zhong Yuanyuan(3)

(E761 Collaboration)

(1) *Fermi National Accelerator Laboratory, Batavia, IL 60510*

(2) *Petersburg Nuclear Physics Institute, Gatchina, Russia*

(3) *Institute of High Energy Physics, Beijing, PRC*

(4) *H.H. Wills Physics Laboratory, University of Bristol, UK*

(5) *Carnegie Mellon University, Pittsburgh, PA 15213*

(6) *University of Iowa, Iowa City, IA 52242*

(7) *Institute of Theoretical and Experimental Physics, Moscow, Russia*

(8) *State University of New York at Albany, Albany, NY 12222*

(9) *Universidade Federal da Paraiba, Paraiba, Brazil*

(10) *Centro Brasileiro de Pesquisas Fisicas, Rio de Janeiro, Brazil*

(11) *Conselho Nacional de Pesquisas CNPq, Rio de Janeiro, Brazil*

(12) *Universidade de São Paulo, São Paulo, Brazil*

(13) *J.W. Gibbs Laboratory, Yale University, New Haven, CT 06511*

(October 3, 1994)

Abstract

We have measured the branching ratio for the hyperon radiative decay, $\Sigma^+ \to p\,\gamma$, using the Fermilab polarized charged hyperon beam. This measurement and our previously published result on the asymmetry parameter in the same decay are part of Fermilab experiment E761. We find $\mathrm{BR}(\Sigma^+ \to p\,\gamma)/\,\mathrm{BR}(\Sigma^+ \to p\,\pi^0)$ to be $(2.32\pm0.11(\mathit{stat.})\pm0.10(\mathit{syst.}))\times10^{-3}$ with a sample of 31901 events. The higher statistics and careful attention to systematic uncertainties make these significant improvements over previous measurements. We describe how our measurements were performed and briefly review the theoretical implications of these results.

PACS numbers: 13.40.Fn, 14.20.Jn

Typeset using REVTEX

---

[*] Present address: Fermi National Accelerator Laboratory, Batavia, IL 60510

[†] Present address: SCIPP, Natural Science II, University of California, Santa Cruz, CA 95064

[‡] Present address Department of Physics, University of Maryland, College Park, MD 20747

[§] Present address: COPPE, Universidade Federal do Rio de Janeiro, Brazil

[**] Present address: Universidade Estadual do Rio de Janeiro, Brazil

[††] Present address: Instituto de Física, Universidad Autónoma de San Luis Potosí, San Luis Potosí, S.L.P. 78240 México.

[‡‡] Present address: Department of Physics, Stanford University, Stanford, CA 94309

I. INTRODUCTION

Hyperon radiative decays represent a class of rare baryon decays which require contributions from both the weak and electromagnetic interactions. The description of these processes in terms of well understood electroweak forces is complicated by the presence of the strong interactions. In his fundamental theorem Hara proved in 1964 [1] that the asymmetries in radiative decays of Σ^+ and Ξ^- vanish in the SU(3) limit, assuming only CP invariance and left-handed currents in the weak interaction. Contrary to this prediction, the first low statistics measurements of the asymmetry parameter in the decay $\Sigma^+ \to p\,\gamma$ performed in bubble chambers [2,3], revealed evidence for large negative asymmetry. This evidence was supported by the first measurement of the $\Sigma^+ \to p\,\gamma$ asymmetry in a counter experiment [4] which yielded a result of $-0.86 \pm 0.13(\text{stat}) \pm 0.04(\text{syst})$ based on 190 events.

The main difficulty in such experiments is separation of the $\Sigma^+ \to p\,\gamma$ radiative decay from the background hadronic decay $\Sigma^+ \to p\,\pi^0$, which is 400 times more abundant and has similar kinematics for the charged particles and also has photons in the final state. Moreover, the asymmetry parameter in the hadronic decay is large and negative ($\alpha_0 = -0.980 \pm 0.016$) [5], which raised the concern that the observed asymmetry in the $\Sigma^+ \to p\,\gamma$ decay might be due to contamination of the radiative decay sample by hadronic decays. In addition, the number of $\Sigma^+ \to p\,\gamma$ events detected in these experiments was small (about 300 total in 3 experiments), which limited sensitivity to systematic errors.

The branching ratio (BR) of $\Sigma^+ \to p\,\gamma$ decays was found to be approximately 1.2×10^{-3} in bubble chamber experiments [2,3,6,7]. These and three counter experiments performed later with higher statistics [4,8,9], yielded the average result $\text{BR}(\Sigma^+ \to p\,\gamma) = (1.25 \pm 0.07) \times 10^{-3}$ [5].

These observations raised wide interest among theorists (see the references in the next section). In spite of the many models that were investigated, the large negative asymmetry and the observed rate of the $\Sigma^+ \rightarrow p\,\gamma$ decay remained an unexplained enigma. Many phenomenological models of other radiative decays use values of the branching ratio and asymmetry parameter for the decay $\Sigma^+ \rightarrow p\,\gamma$ as input parameters. Thus it was important to carry out a new experiment and to obtain the values of the branching ratio and the asymmetry parameter for the decay $\Sigma^+ \rightarrow p\,\gamma$ with high statistical accuracy and low systematic errors.

This experiment (E761) was designed to meet that challenge. The high energy hyperon beam at Fermilab provided a large flux ($\sim$ 2000/s) of Σ^+ with a polarization of 12%. The direction of the polarization was periodically reversed to allow the separation of the asymmetry from instrumental biases. To identify the $\Sigma^+ \rightarrow p\,\gamma$ decay we used charged particle spectrometers that provided high-precision measurements of the missing neutral mass. In addition, a special photon spectrometer was constructed to determine the direction and energy of the photons. The result was a high statistics data set with low systematic errors and large signal/background ratios for this rare decay.

These measurements were the main thrust of an experiment designed to study radiative decays of hyperons performed in a polarized charged hyperon beam at Fermilab. E761 has also reported the measurements of the branching ratios of the radiative decays $\overline{\Sigma}^- \rightarrow \overline{p}\,\gamma$ [10] and $\Xi^- \rightarrow \Sigma^-\,\gamma$ [11] as well as an upper limit on the branching ratio of $\Omega^- \rightarrow \Xi^-\,\gamma$ [12].

This paper presents results of the measurement of the branching ratio for the radiative decay $\Sigma^+ \rightarrow p\,\gamma$, and a detailed description of the result for the asymmetry parameter which was briefly reported earlier [13]. Available experimental data and a short review of the theory status are presented in the next section. Section III describes experimental layout, trigger logic and data acquisition. Section IV explains the techniques used to reconstruct charged tracks and to separate single photons from neutral pions. The analysis of the data for the asymmetry parameter and for the branching ratio is reported in section V. Section VI concludes the paper.

II. EXPERIMENTAL AND THEORETICAL REVIEW

A. Experimental data

There are eight electroweak ($\Delta S = 1$) radiative decays for hyperons: $\Sigma^+ \to p\,\gamma$, $\Lambda \to n\,\gamma$, $\Sigma^0 \to n\,\gamma$, $\Xi^- \to \Sigma^-\,\gamma$, $\Xi^0 \to \Sigma^0\,\gamma$, $\Xi^0 \to \Lambda\,\gamma$, occur within the spin $(\frac{1}{2})^+$ octet, $\Omega^- \to \Xi^-\,\gamma$ is a transition from the spin $(\frac{3}{2})^+$ decuplet into the spin $(\frac{1}{2})^+$ octet and $\Omega^- \to \Xi^*(1530)^-\,\gamma$ occurs within the spin $(\frac{3}{2})^+$ decuplet. The decay $\Sigma^0 \to n\,\gamma$ is experimentally inaccessible because it is overwhelmed by the purely electromagnetic transition $\Sigma^0 \to \Lambda\gamma$. The decay $\Omega^- \to \Xi^*(1530)^-\,\gamma$ will be hard to measure in the near future because it has less phase space than the decay $\Omega^- \to \Xi^-\,\gamma$ which has not yet been observed.

Table I presents the current experimental data on the branching ratios and asymmetry parameters of the radiative hyperon decays including the results of the present experiment. The absolute branching ratios are given. Most of the experiments have measured the branching ratios relative to some other decay and their results are converted with use of the corresponding data from the Particle Data Group [5]. We also show the observed number of events in every experiment. If the asymmetry measurement is based on a different number of events than the branching ratio measurement in the same experiment, that number of events is shown in parentheses.

TABLES

TABLE I. Summary of results on the branching ratio and asymmetry parameter measurements for the hyperon radiative decays

No. of Events	Branching Ratio (10^{-3})	Asymmetry Parameter	Laboratory	Reference, Year
		$\Sigma^+ \rightarrow p\,\gamma$		
24	1.91 ± 0.41		BNL	Bazin [7] (1965)
31 (61)	1.42 ± 0.26	$-1.03^{+0.52}_{-0.42}$	Berkeley	Gershwin [2] (1969)
45	1.08 ± 0.15		CERN	Ang [6] (1969)
30 (46)	1.09 ± 0.20	$-0.53^{+0.38}_{-0.36}$	CERN	Manz [3] (1980)
155	$1.27^{+0.15}_{-0.18}$		CERN	Biagi [9] (1985)
190	1.30 ± 0.15	$-0.86 \pm 0.13 \pm 0.04$	KEK	Kobayashi [4] (1987)
408	$1.45 \pm 0.20^{+0.11}_{-0.22}$		BNL	Hessey [8] (1989)
(34754)		$-0.720 \pm 0.086 \pm 0.045$	Fermilab	†Foucher [13] (1992)
31901	$1.20 \pm 0.06 \pm 0.05$		Fermilab	†This result
		$\Xi^- \rightarrow \Sigma^-\,\gamma$		
11	0.23 ± 0.10		CERN	Biagi [14] (1987)
211	$0.122 \pm 0.023 \pm 0.006$	1.0 ± 1.3	Fermilab	†Dubbs [11] (1994)
		$\Xi^0 \rightarrow \Sigma^0\,\gamma$		
85	$3.56 \pm 0.42 \pm 0.10$	$0.20 \pm 0.32 \pm 0.05$	Fermilab	Teige [15] (1989)
		$\Xi^0 \rightarrow \Lambda\,\gamma$		
116 (87)	$1.06 \pm 0.12 \pm 0.11$	0.43 ± 0.44	Fermilab	James [16] (1990)
		$\Lambda \rightarrow n\,\gamma$		
24	1.02 ± 0.33		CERN	Biagi [17] (1986)
287	$1.78 \pm 0.24 \pm 0.15$		BNL	Noble [18] (1992)
1816	1.75 ± 0.15		BNL	Larson [19] (1993)
		$\Omega^- \rightarrow \Xi^-\,\gamma$		

Limits at 90% CL

< 2.2	CERN	Bourquin [20] (1984)
< 0.46	Fermilab	†Albuquerque [12] (1994)

†indicates results of this experiment

In 1985 when this experiment was approved the experimental data on $\Sigma^+ \rightarrow p\,\gamma$ decay were meager and came from four bubble chamber experiments (Bazin *et al* [7], Gershwin *et al* [2], Ang *et al* [6], and Manz *et al* [3]) which used low energy $K^-\,p$ interactions to produce Σ^+ for the study of Σ^+ radiative decays. The signal from radiative decay was isolated using the high resolution of the bubble chambers. In spite of low statistics, two of these groups [Gershwin and Manz] were able to give the first indication of large and negative asymmetry in the $\Sigma^+ \rightarrow p\,\gamma$ decay owing to significant (about 40%) production polarization of Σ^+ in low energy $K^-\,p$ interactions.

Counter experiments have led to further progress. The CERN SPS hyperon beam experiment WA42 (Biagi *et al*, [9]) has reported the measurement of the branching ratio of $\Sigma^+ \rightarrow p\,\gamma$ with as much statistics as in the previous four bubble chamber experiments. The first measurement of the asymmetry parameter with a counter technique was done by Kobayashi *et al* [4]. They used a 1.7 GeV/c π^+ beam to produce highly-polarized (87%) Σ^+ in $\pi^+ p$ interactions. The measured direction of the photon in their apparatus was used as well as the missing mass resolution to isolate the $\Sigma^+ \rightarrow p\,\gamma$ signal. The largest previous sample of $\Sigma^+ \rightarrow p\,\gamma$ events was collected in a counter experiment at BNL in the measurement of the branching ratio (Hessey *et al* [8]). BNL experiment E811 (Larson *et al* [19]) collected the largest sample of neutral hyperon radiative decays, measuring 75 times more $\Lambda \rightarrow n\,\gamma$ decays than the previous world total (the result of Noble *et al* [18] is included in [19]).

The counter technique and high intensity hyperon beams at CERN and Fermilab made possible the measurements of radiative decays of neutral hyperons ($\Lambda \rightarrow n\,\gamma$, Biagi *et al* [17], $\Xi^0 \rightarrow \Sigma^0\,\gamma$, Teige *et al* [15], and $\Xi^0 \rightarrow \Lambda\,\gamma$, James *et al* [16]). Hyperon beams also allowed the first measurement of $\Xi^- \rightarrow \Sigma^-\,\gamma$, with branching ratio well below 10^{-3}, (Biagi *et al*, [14]) and setting an upper limit for $\Omega^- \rightarrow \Xi^-\,\gamma$ (Bourquin *et al*, [20]). Table I also includes our results from E761 for $\Xi^- \rightarrow \Sigma^-\,\gamma$ [11] and our improved upper limit for $\Omega^- \rightarrow \Xi^-\,\gamma$ [12].

B. Theory review

The transition matrix element, T, for a general radiative decay of a hyperon Y of momentum p to a baryon B of momentum p' and a photon γ of momentum q,

$$Y(p) \rightarrow B(p') + \gamma(q) \tag{1}$$

is given by (2)

$$T = G_F \frac{e}{\sqrt{4\pi}} \epsilon_\nu \overline{u}(p')(A + B\gamma_5)\sigma_{\mu\nu} q_\mu u(p) \tag{2}$$

where $\overline{u}(p')$ and $u(p)$ are the spinor wave functions of the baryon and hyperon respectively, ϵ_ν is the polarization vector of the photon, A and B are the parity conserving and parity violating amplitudes, and $\sigma_{\mu\nu}$ and γ_5 are combinations of Dirac gamma matrices, G_F is the Fermi constant, and e is the electron charge.

In experiment E761 we measure the branching ratio $BR \propto \mid A \mid^2 + \mid B \mid^2$ and the asymmetry parameter $\alpha = 2Re(A^*B)/(\mid A \mid^2 + \mid B \mid^2)$. For a polarized hyperon, the differential center of mass angular distribution of number of events N is given by:

$$\frac{dN}{d\Omega} = \frac{N_0}{4\pi}(1 + \alpha \mathbf{P} \cdot \hat{\mathbf{n}}) \tag{3}$$

where $\mathbf{P}$ is the polarization vector of the hyperon Y, N_0 is the total number of events, and $\hat{\mathbf{n}}$ is a unit vector in the direction of the outgoing baryon in the hyperon rest frame.

Since 1956 [21] the hyperon radiative decays have been a test arena for many theoretical models (condensed lists of references are available [22,23] as well as a review article [24]). None of them have given a completely self-consistent picture of these phenomena. Among widely used theoretical approaches were the pole model, quark transition mechanisms, unitarity and symmetry principles.

The most theoretically reliable information about branching ratios is the set of lower bounds for the branching ratios obtained on the basis of the unitarity principle (Table II). Unitary lower bounds are calculated by estimating the imaginary part of the amplitudes from experimental data of related reactions. For the $\Sigma^+ \to p\,\gamma$ decay it was shown that in spite of a large dispersion of estimates [25–27] the contribution of the imaginary part of the amplitudes to the branching ratio was small, and thus the decay is dominated by real amplitudes. In contrast, the unitarity lower bounds of the branching ratios for $\Lambda \to n\,\gamma$ [25,26] and $\Xi^- \to \Sigma^-\,\gamma$ [25,27] decays are close to experimental results. Kogan and Shifman combined an estimate of the real part of the amplitudes with the imaginary part used for the lower bounds, and predicted BR($\Xi^- \to \Sigma^-\,\gamma$) $\sim 0.17 \times 10^{-3}$ and BR($\Omega^- \to \Xi^-\,\gamma$) = $(0.01\text{–}0.015)\times 10^{-3}$ [27]. Note that as we can see from Table I, the new experimental result [11] for BR($\Xi^- \to \Sigma^-\,\gamma$) is two standard deviations lower than the estimate and consistent with the unitarity lower bound itself, possibly indicating an overestimation of the real part. Our new upper limit for BR($\Omega^- \to \Xi^-\,\gamma$) [12] is still significantly above the estimated unitarity lower bound [27].

TABLE II. Unitarity lower bounds for branching ratios, in 10^{-3}

Author	$\Sigma^+ \to p\,\gamma$	$\Lambda \to n\,\gamma$	$\Xi^- \to \Sigma^-\,\gamma$	$\Omega^- \to \Xi^-\,\gamma$
Zakharov [25]	(0.066±0.039)	0.83	0.13	
Farrar [26]	0.0069	0.85		
Kogan [27]	0.03		0.1	0.008

The first phenomenological attempt to calculate a branching ratio and asymmetry parameter for hyperon radiative decays [28,29] was the pole model, which had already been applied to hyperon non-leptonic decays [30]. In this model the radiative decay is separated into a weak vertex, H_W, and an electromagnetic vertex, connected through intermediate hyperon states Y' or baryon states B'. Figure 1A shows a sample diagram with a B' state. Various calculations employed different intermediate states, including the lowest lying $(\frac{1}{2})^+$ baryons [26], the $(\frac{3}{2})^+$ states [31,32], the $(\frac{1}{2})^+$ $(56,0^+)$ states for the parity-conserving amplitude and the $(\frac{1}{2})^-$ $(70,1^-)$ states for the parity violating amplitude [33–35]. A K* pole diagram with low mass vector mesons was used in [36]. Summaries of the pole model predictions for the branching ratios and asymmetry parameters of hyperon radiative decays are presented in Table III and IV respectively.

TABLE III. The pole model predictions for the branching ratios of radiative decays of hyperons (units of 10^{-3})

Author	$\Sigma^+ \to p\,\gamma$	$\Lambda \to n\,\gamma$	$\Xi^0 \to \Lambda\,\gamma$	$\Xi^0 \to \Sigma^0\,\gamma$	$\Xi^- \to \Sigma^-\,\gamma$
Graham [29]	1.4	0.75	0.3	1.1	0.02
Farrar [26]	0.34±1.25	1.9±0.8			
Scadron [31]	0.78	1.5	15.	10.	0.
Gavela [33]	$0.92^{+0.26}_{-0.14}$	0.62	3.	7.2	
Rauh [35]	$0.82^{+0.41}_{-0.31}$	1.02	2.29	5.87	
Scadron [32]	0.66				
Nardulli [36]	1.05	0.17	0.72	2.4	0.51

TABLE IV. The pole model predictions for the asymmetry parameters of radiative decays of hyperons

Author	$\Sigma^+ \to p\,\gamma$	$\Lambda \to n\,\gamma$	$\Xi^0 \to \Lambda\,\gamma$	$\Xi^0 \to \Sigma^0\,\gamma$	$\Xi^- \to \Sigma^-\,\gamma$
Graham [29]	+0.061	+0.25	−0.25	+0.031	−0.37
Farrar [26]	$+0.8^{+0.2}_{-1.1}$	−0.5±0.4			
Scadron [31]	−0.35 ± 0.15	−0.995	−0.95	−0.90	0.
Close [34]	−0.8 ± 0.2	small	small	−0.3	
Gavela [33]	$-0.8^{+0.32}_{-0.19}$	−0.49	−0.78	−0.96	
Rauh [35]	$-0.86^{+0.11}_{-0.13}$	−0.10	−0.41	−0.58	
Scadron [32]	−0.38				
Nardulli [36]	−1.0	−0.72	+0.11	−0.54	0.

The comparison of the pole model predictions with experimental results (Table I) shows that it does not give a unified picture of the hyperon radiative decays. Some pole model calculations were consistent with the existing data on branching ratio and asymmetry parameter for $\Sigma^+ \to p\, \gamma$ [33,35], but their predictions for the radiative decays of Ξ^0 gave branching ratios two to three times too large and the wrong sign of the asymmetry parameters. The weakness of this approach is that it presents only a phenomenological description of the processes and its predictive power suffers from an arbitrary choice of intermediate states.

The idea of relating hyperon non-leptonic and radiative decays was used in another phenomenological consideration—a combined symmetry and vector dominance model—by Żenczykowski [22,37] to describe the branching ratios and asymmetry parameters for all hyperon radiative decays except $\Omega^- \to \Xi^-\, \gamma$. The data on non-leptonic decays of the hyperons fix two of the three parameters in the parity violating amplitudes. The third parameter is determined by a fit to the data of the measurements of hyperon radiative decays. The model successfully describes the data with its largest deviation being in the asymmetry parameter of $\Xi^0 \to \Sigma^0\, \gamma$. Positive asymmetry parameters are predicted for $\Lambda \to n\, \gamma$ (+0.83) and $\Xi^- \to \Sigma^-\, \gamma$ (+0.59) decays.

The general success of the quark model in prediction of the baryon magnetic moments and its description of the electromagnetic decays of mesons and baryons led to the use of quark-based considerations to attempt to describe the weak radiative decays. In the work of Gilman and Wise [38] the general assumption is made that the radiative decays originate from a strange quark making a weak transition into a down quark with emission of a photon from a short distance: $s \to d\gamma$ as in Figure 1B. The other two quarks in the hyperon are considered spectators. The relative radiative weak decay rates of the hyperons are calculated using the $\Sigma^+ \to p\, \gamma$ rate as input. Their results fail to reproduce the relative rates of the radiative decays. Under this scheme all radiative decays should have the same value of the asymmetry parameter. The authors concluded that the single-quark transition as the dominant mechanism has to be ruled out and other contributions are necessary. They could be two- and three-quark transition diagrams.

A estimate of the absolute rate for $\Sigma^+ \rightarrow p\ \gamma$ decay assuming the single-quark transition $s \rightarrow d\gamma$ was made by Kogan and Shifman [27]. The branching ratio was found to be 2 $\times\ 10^{-6}$, about 3 orders of magnitude below the experimentally measured value. These authors concluded that the local single-quark transition cannot play an important role in weak radiative decay.

The internal W-exchange two-quark transitions shown in Figure 1C can contribute to all hyperon radiative decays except $\Xi^- \rightarrow \Sigma^-\ \gamma$, $\Omega^- \rightarrow \Xi^-\ \gamma$, and $\Omega^- \rightarrow \Xi^*(1530)^-\gamma$ since these initial hyperons contain no valence u quark needed to keep charge conserved in W^- exchange. A calculation of the two-quark transition amplitudes predicted [39] an asymmetry parameter for $\Sigma^+ \rightarrow p\ \gamma$ of -0.154, much smaller in magnitude than the experimentally measured value.

The combined effect of single-quark and two-quark transitions was calculated [40,41] using $\Sigma^+ \rightarrow p\ \gamma$ and $\Xi^- \rightarrow \Sigma^-\ \gamma$ data as input. The calculated values were not in agreement with data for $\Xi^0 \rightarrow \Sigma^0\ \gamma$ and $\Xi^0 \rightarrow \Lambda\ \gamma$ decays. The predicted branching ratios were consistent with data when they included long-distance effects in combination with short-distance QCD. This model predicts an asymmetry parameter for $\Sigma^+ \rightarrow p\ \gamma$ of -0.59, but its prediction of $\alpha\ \sim -0.90$ for $\Xi^0 \rightarrow \Sigma^0\ \gamma$ disagrees with the measured asymmetry parameter of (0.20±0.32) [15].

Uppal and Verma [42] investigated the single- and two-quark transitions in the framework of the quark-diquark model and SU(6) symmetry breaking. With BR($\Sigma^+ \rightarrow p\ \gamma$) as input, they observed that better agreement with most branching ratios and asymmetries could be obtained with SU(6) breaking of 10 degrees and increasing the BR($\Xi^- \rightarrow \Sigma^-\ \gamma$) to 0.5 $\times\ 10^{-3}$. They also predicted BR($\Omega^- \rightarrow \Xi^-\ \gamma$) of $1.8\times\ 10^{-3}$. The latest results on these decays do not support the increase in BR($\Xi^- \rightarrow \Sigma^-\ \gamma$) needed to obtain this better agreement, and strongly reject the prediction for $\Omega^- \rightarrow \Xi^-\ \gamma$.

The penguin diagrams, which have one or more gluon lines connecting the quarks (Figure 1D) and in addition a photon being emitted from one of the quark lines, can contribute to all radiative decays. Penguin diagrams were originally thought [43] to play an important role in hyperon non-leptonic decays ($\Delta I = 1/2$ rule) and in the ϵ'/ϵ ratio of neutral kaon decays.

Kamath [44] and Eeg [45] calculated the contribution of the penguin diagrams in **Figure 1D** to the branching ratios of $\Xi^- \rightarrow \Sigma^- \gamma$ and $\Omega^- \rightarrow \Xi^- \gamma$ and predicted a BR($\Omega^- \rightarrow \Xi^- \gamma$) of 10^{-4} - 10^{-5} and BR($\Xi^- \rightarrow \Sigma^- \gamma$) of 10^{-7} - 10^{-8}, in large disagreement with the experimental value of BR($\Xi^- \rightarrow \Sigma^- \gamma$). The contribution of a similar penguin diagram to the BR($\Sigma^+ \rightarrow p\, \gamma$) was found to be negligible [46].

Several calculations of rate and asymmetry parameter have been done recently using the QCD sum rules approach (Table V). The first calculations by Khatsymovsky [47,48] and Balitsky *et al* [49] yielded a large positive asymmetry parameter in $\Sigma^+ \rightarrow p\, \gamma$ decay [50]. Goldman and Escobar [51] analyzed, using the method of the QCD sum rules, only the short-distance contribution $s \rightarrow d\gamma$ to the $\Sigma^+ \rightarrow p\, \gamma$ and $\Xi^- \rightarrow \Sigma^- \gamma$ decays. The branching ratios, while still smaller than the experimental data, are larger than those obtained by the early single-quark calculations [27]. They obtained an asymmetry parameter for $\Sigma^+ \rightarrow p\, \gamma$ decay $\alpha = -1.0$. Balitsky, Braun and Kolesnichenko [52] have developed some new techniques for the construction of QCD sum rules for hadronic amplitudes in alternating external fields, taking into account higher twist corrections than the previous work [47,49], and have been able to obtain a sum rule for $\Sigma^+ \rightarrow p\, \gamma$ which yields the branching ratio and the asymmetry parameter in close agreement with the current experimental results. However, their approach has not been extended to other weak radiative decays.

TABLE V. QCD sum rule predictions for branching ratios (in units of 10^{-3}) and asymmetry parameters of hyperon radiative decays

Reference	$\Sigma^+ \to p\,\gamma$	$\Xi^- \to \Sigma^-\,\gamma$	$\Xi^0 \to \Lambda\,\gamma$	$\Lambda \to n\,\gamma$	$\Omega^- \to \Xi^-\,\gamma$
			Branching ratios		
Khatsymovsky [47]	0.8	0.20			0.23
Khatsymovsky [48]			1.1	2-3	
Balitsky [49]	2.5				
Goldman [51]	0.047	0.002			
Balitsky [52]	0.5-1.5				
			Asymmetry parameters		
Khatsymovsky [47]	+1.0	+0.4			
Khatsymovsky [48]			+0.9	+0.125 ± 0.025	
Balitsky [49]	+0.8				
Goldman [51]	−1.0	+0.9			
Balitsky [52]	−0.85±0.15				

Jenkins *et al* [53] have recently given an analysis of hyperon radiative decays using chiral perturbation theory (see also Neufeld [54]). In this theory the real part of the parity-conserving amplitude was treated as a free parameter. Their results are consistent with experimental data with the exception that they predict a small asymmetry parameter for $\Sigma^+ \to p\,\gamma$ decay.

The large negative asymmetry of $\Sigma^+ \to p\,\gamma$ is unexpected given the relatively small breaking of the SU(3) symmetry of flavor. Hara's theorem holds strictly only in the case of exact SU(3) flavor symmetry. In this limit, the parity-violating amplitudes of $\Sigma^+ \to p\,\gamma$ and $\Xi^- \to \Sigma^-\,\gamma$ decay vanish and the asymmetry parameters are zero. Matinyan proved in the limit of SU(6) symmetry the asymmetries of all hyperon decays belonging to the spin $(\frac{1}{2})^+$ octet (all hyperons except Ω^-) are zero [55]. Gourdin showed that U-spin symmetry in the U-spin doublets (Σ^+, p) and (Ξ^-, Σ^-) is sufficient to make the parity-violating amplitudes vanish [56]. Vasanti made an early estimate [57] that the SU(3) symmetry breaking effects would yield the asymmetry parameter (4).

$$\alpha = \frac{m_s^2 - m_d^2}{m_s^2 + m_d^2} \tag{4}$$

For the constituent quark masses m_s=450 MeV and m_d=300 MeV this gives α_γ=+0.38.

In an effort to explain the discrepancy between theory and experiment, some theorists have suggested reasons why the assumptions behind the theorem are not true [58] (also see comments [59] on this critique). Others have constructed models which incorporate explicit violation of the Hara theorem even in the SU(3) limit [22,60]. These arguments stand in contrast to the calculation of Balitsky *et al* [52] which does not incorporate explicit violation of Hara's theorem and obtains a large negative asymmetry parameter. In the SU(3) limit that calculation yields a rate that is an order of magnitude lower and a zero asymmetry parameter for $\Sigma^+ \to p\,\gamma$.

The question that remains to be answered is not whether the predictions of Hara's theorem are violated but why and how they are violated. To conclude this section we discuss this point in more detail.

Surely, the flavor SU(3) symmetry is violated. Otherwise the octet baryons could not decay at all. But its violation has two different manifestations. The first and most obvious effect is kinematical, giving rise to mass differences which in turn provide phase space to make the decays possible. The other effect is the SU(3) symmetry violation effects in transition amplitudes, and it is in these transition amplitudes that Hara's theorem is acting or violated.

The role of the flavor symmetry has been studied in various cases. Sometimes its violation can be neglected or treated in a perturbation-like manner. The well known example is the Gell-Mann–Okubo formula for masses in the unitarity multiplets. Another example is SU(3) relation between amplitudes for semileptonic decays of the octet baryons [61,62].

In contrast, there is non-perturbative symmetry violation in the baryon magnetic moments and the transition magnetic moments for meson radiative decays. However, in this case, there exists a simple picture that gives a satisfactory description for the magnetic moments without being involved in complications related to non-perturbative corrections. This is the model of quasi-free constituent quarks with Dirac magnetic moments.

Weak radiative decays show a different type of flavor symmetry violation. Here the perturbative-like approaches tend to give positive asymmetry for the $\Sigma^+ \to p\,\gamma$ decay [57] and hence are inadequate. The failure of this approach and other simple descriptions might be understood by examining chirality considerations [24,51]. Only left-handed quarks participate in the standard weak interaction while normal electromagnetic interaction does not change handedness (chirality). On the other hand, the quark description of weak radiative decays requires participation of at least one (initial or final) right-handed quark. Therefore, one needs to reverse somehow the quark chirality. The simplest and quite familiar way is to include quark masses into consideration. Then the natural expectation is that the higher s-quark mass produces a stronger effect and thus violates Hara's theorem, but this leads to positive asymmetry in $\Sigma^+ \to p\,\gamma$ decay.

QCD sum rules may suggest a new possibility [24]—chirality can be reversed due to influence of the vacuum condensate. Here the usual guess is that the quark pair density in the condensate should be larger for the lighter quarks. Then the vacuum condensate contribution makes favorable participation of the right-handed quarks in the final state (where only lighter quarks are present). Thus we have two competing contributions (mass or condensate) which allow us to get the negative asymmetry in accordance with experiment. Thus the QCD sum rules approach and its claimed success by Balitsky, Braun and Kolesnichenko [52] in describing the $\Sigma^+ \rightarrow p\ \gamma$ decay may appear promising. Further theoretical and experimental work is needed to clear up the physics of the radiative decays.

III. EXPERIMENTAL LAYOUT

The experiment was located in the Proton Center beam line at Fermilab. The apparatus (Figure 2) had four parts: the charged hyperon beam line and three spectrometers, one each for the incident hyperon (Y), decay baryon (B), and a photon (photons) in a generic hyperon radiative decay $Y \rightarrow\ B\ \gamma$ or a hadronic decay $Y \rightarrow B\ \pi^0$, $\pi^0 \rightarrow \gamma\gamma$.

A. Polarized Charged Hyperon Beam

The 800 GeV/c proton beam in the Proton Center beam line was focused onto the hyperon production target. The targeting angle of the protons could be varied over the range ± 5 mrad. The beam spot size was 0.5 mm horizontally and 1 mm vertically at the target. During the E761 run the intensity of the proton beam was $6 - 8 \times 10^{11}$ protons/spill on the target. The beam spill was 23 s long and occured every 57 s (40% duty factor).

The one interaction length (15 cm long) Cu target was located in the upstream end of the hyperon magnet. It was 2 mm high and 0.5 mm wide. The narrow horizontal extent contributed to the excellent momentum resolution of the produced hyperons.

The hyperon beam was selected in momentum and collimated by the narrow curved channel [63] embedded within the hyperon magnet. The hyperon magnet is a 7.3 m long dipole magnet which was operated at a field of 3.5 T in the vertical plane and imparted a transverse momentum $\Delta p_t = -7.5$ GeV/c to the 375 GeV/c secondary hyperon beam. The size of the beam at the exit of the hyperon magnet was determined by the size of the channel exit and was 0.36 cm in X (horizontal) and 0.9 cm in Y (vertical). The beam had a momentum spread of $\Delta p/p = 8\%$ full width at half maximum, and a solid angle of 0.64 μsr. The fraction of Σ^+ in the beam at the beginning of the decay volume was 1.3%, with the rest mostly protons and pions.

The polarized Σ^+ hyperons were produced in the inclusive reaction $p + Cu \rightarrow \Sigma^+ + X$ by steering the incoming proton beam onto the production target at a finite production angle (the targeting angle). According to the convention [64] a positive polarization is in the same direction as the cross product of the incident beam direction with the produced hyperon direction. In our experiment, data were taken with equal and opposite horizontal targeting angles near 3.7 mrad. Because of our right-handed coordinate system, a positively polarized particle such as the Σ^+ has spin down at positive targeting angles and spin up at negative angles. We will refer to the samples taken at +3.7 mrad as POS and the –3.7 mrad sample as NEG throughout this paper. The average magnitude of polarization of the two sets was 12%.

B. Hyperon and Baryon Spectrometers

Σ^+ hyperons at 375 GeV/c have a mean decay length of 7.6 m. This allowed us to measure the trajectory of the Σ^+ hyperon with high precision in a magnetic hyperon spectrometer before its decay. The hyperon spectrometer consisted of 9 planes of 50 μm pitch silicon strip detectors, arranged in three stations, SSD1 - SSD3, and a 2 m long magnet with $\Delta p_t = 1.43$ GeV/c. The total amount of material in the hyperon spectrometer was 7.5% of a radiation length (L_r). Hyperon trajectories were measured with momentum resolution (σ_p/p) of 0.7% and angular resolution (σ) of 12 and 5 μrad for horizontal and vertical angles, respectively. The measured hyperon trajectory could be extrapolated through the hyperon magnet to distinguish particles emerging from the target from background caused by interaction in the channel walls.

The baryon spectrometer was used to measure the proton trajectory. It included 30 planes of multiwire proportional chambers (PWC's) assembled in four stations, each containing four views. The first three stations PWC A, B and C had 8 planes each of 1 mm pitch chambers while the last station PWC D had 6 planes of 2 mm pitch chambers. The baryon spectrometer magnet consisted of three 2 m long magnets powered in series, with combined $\Delta p_t = -2.46$ GeV/c. The momentum resolution (σ_p/p) of the baryon spectrometer was 0.2%. The angular resolution (σ) was 9 μrad in horizontal angle and 6 μrad in vertical angle.

The length of the decay region between the two spectrometers, namely from SSD3 to the station PWC A, was 14 m. The region between SSD3 and the photon spectrometer was filled with helium gas in polyethylene bags to reduce the effects of multiple Coulomb scattering and interactions that could produce photon triggers. The aperture of the station PWC A was designed to be big enough to allow photons from a decay to go through without interaction in the material of the PWC A frames. The amount of material from the beginning of the decay region at SSD3 to the end of PWC D, including the PWC's and TRD's, corresponded to 22.8% L_r.

We can separate the decays $\Sigma^+ \rightarrow p\ \gamma$ and $\Sigma^+ \rightarrow p\ \pi^0$ by calculating the missing neutral mass squared ($M^2_{X^0}$) from the measured momenta in the hyperon and baryon spectrometer with the hypothesis that the hyperon is a Σ^+ and the baryon is a proton. The design of both spectrometers was optimized in a Monte Carlo simulation with the goal of obtaining the best possible resolution in $M^2_{X^0}$ and maximizing the acceptance. The Monte Carlo simulation indicated that resolution (σ) in $M^2_{X^0}$ would be 0.0026 GeV^2/c^4, enough for a seven standard deviation separation between π^0 ($M^2_{X^0}$=0.0182 GeV^2/c^4) and γ ($M^2_{X^0}$=0.0 GeV^2/c^4) if the $M^2_{X^0}$ distributions were Gaussian. The experimental values of resolution in $M^2_{X^0}$ proved to be comparable to the expected resolution. However, as also expected, the data showed non-Gaussian contributions in the tails of $M^2_{X^0}$ distribution making this separation much less clear. Further reduction of the background of hadronic decays was achieved using the photon spectrometer.

C. Photon Spectrometer

The photon spectrometer (Figure 3) consisted of a set of tracking transition radiation detectors (TRD's) to measure the position of the photon and a photon calorimeter to measure the photon energy. There was a 7.6 × 7.6 cm^2 hole in the massive parts of the photon spectrometer to allow the undecayed beam and the protons through. The photons that went through this hole were measured in a rear lead glass array.

The coordinate part of the photon spectrometer was made of two identical sections, each of which had a steel converter, a proportional wire chamber (PWC) and two tracking transition radiation detectors (TRD). This novel application of a TRD combined with a gamma converter for measuring the coordinates of high energy photons was tested in a separate preliminary experiment [65]. The main idea was to select only high energy electrons (positrons) in the electromagnetic showers as they retain well the initial direction of the incident photon, while low energy electrons (positrons) have a much wider angular distribution. The TRD is chosen because it is a threshold detector. It detects with high efficiency electrons (positrons) with energies above 2.5 GeV and it is practically insensitive to electrons with energies less than 1 GeV. The average energy of the photon from the $\Sigma^+ \to p\,\gamma$ decay was 50 GeV. Photons were converted in either of two 2.54 cm thick steel plates (1.54 L_r each) producing electromagnetic showers. Steel was used as a converter material instead of lead because self-support and uniform thickness could be more easily achieved.

Each TRD consisted of a polypropylene multifoil radiator and a special xenon proportional wire chamber with 2 mm wire spacing, filled with a gas mixture of 70% Xe and 30% CH_4 with thickness of 16 mm. The high energy electrons (positrons) produced transition radiation X-rays in the radiator. The X-rays were detected with high efficiency in the xenon proportional wire chamber, and were recorded with the cluster-counting method [66,67]. The electron response of these TRD's was known from their use in a previous experiment for electron detection [68]. PWC planes with 2 mm wire spacing, similar to those in the baryon spectrometer, were used to supplement the information from the TRD. There were 8 planes of PWC and TRD in the photon spectrometer. The active area of these chambers was 57.6 × 57.6 cm^2. The coordinate resolution of the photon spectrometer was 2 mm (FWHM).

The photon energy was measured in a photon calorimeter which consisted of three arrays: front lead glass, main lead glass and BGO ($Bi_4Ge_3O_{12}$) crystals (Figure 4). The front and main arrays consisted of blocks of F2 type glass, 10 × 10 × 38.4 cm^3 each. The front array had the long axis transverse to the beam (3.15 L_r) and the main array's long axis was parallel to the beam (12 L_r). BGO crystals were used to line the 12.5 × 12.5 cm^2 hole to contain showers that originated closer to the hole. The crystals were 2.5 × 2.5 × 20 cm^3 (18 L_r). A rear lead-glass array of four blocks 20 × 20 × 40 cm^3 (12.5 L_r) covered the angular region for photons that went through the hole.

Since the total amount of energy observed in the calorimeter is similar for $\Sigma^+ \rightarrow p\ \gamma$ and $\Sigma^+ \rightarrow p\ \pi^0$ decays, position resolution is more important than energy resolution in separating them. We require a large percentage of the total energy observed in the calorimeter to be within 5 cm of the predicted positition of the neutral track (see section IV. B.) This takes full advantage of the position resolution while lessening our dependence on the energy resolution of the calorimeter. The energy resolution of the photon calorimeter was $\sigma/E = 30\%/\sqrt{E}$ + 3% constant term added in quadrature. This modest resolution was due in part to having only 18 L_r of material, of which the first 3 were passive steel plates. Some of the total energy escaped into the hole in the center of the calorimeter and out the sides.

D. Trigger and Data Acquisition

The trigger consisted of three levels and was designed to require all three particles in the decay $\Sigma^+ \rightarrow p\ \gamma$, making no significant difference at the on-line level between $\Sigma^+ \rightarrow p\ \gamma$ and $\Sigma^+ \rightarrow p\ \pi^0$ decays. The first level trigger, T1, was a coincidence of three scintillation counters (not shown on Figure 2), located in the hyperon spectrometer at each SSD station and covering the phase space of the beam exiting the hyperon magnet channel. The T1 trigger rate was 10^5 Hz.

The T2 trigger was T1 and a trigger on photons converted in one of the two steel plates of the photon spectrometer (Figure 3):

$$\mathrm{T2} = \mathrm{T1} * [(\overline{\mathrm{V1}} * \mathrm{S1}) + (\overline{\mathrm{V1}} * \overline{\mathrm{V2}} * \mathrm{S2})] \tag{5}$$

By requiring no signal in the veto counters (V1 and V2 of Figure 3) upstream of the steel plates, and a signal in S1 or S2 downstream of the plates, we selected only those events where photons convert inside the steel and prevent triggers from particles converting outside the steel. If neither S1 nor S2 gave a trigger, then we allowed a trigger if there was energy in the rear lead glass. These triggers were prescaled by 1:4. These rear photon triggers were later excluded from the branching ratio analysis. The rate of the T2 trigger was about 1.4% of the beam rate (T1).

The third level trigger T3 caused the readout of the event. It required a high momentum proton from the decay $\Sigma^+ \rightarrow p\ \gamma$ or $\Sigma^+ \rightarrow p\ \pi^0$. The kinematics of these decays is similar and the phase spaces of protons overlap for both decays. The corresponding scintillation counter P was placed behind the proportional wire chambers PWC D, on the expected proton trajectory. The level T3 trigger also required a minimum energy of $\mathrm{E} > 5$ GeV on the energy deposited in the photon calorimeter or the rear lead glass array:

$$\mathrm{T3} = (\mathrm{T2} * \mathrm{P} * \mathrm{E} > 5\mathrm{GeV}) + \mathrm{T1}_{Pr} \tag{6}$$

This reduced triggers where a low energy photon was produced in an interaction. The trigger T3 also required the beam particle to be the only particle within a 400 ns time window, ensuring that no other particles went through the apparatus during the drift time of the TRD. The component $\mathrm{T1}_{Pr}$ was the beam trigger T1 prescaled by 1:8192 and comprised about 1% of all T3 triggers. It was used for alignment and detector studies. The rate of T3 triggers was 0.6% of the beam rate. 24% of those triggers reconstructed as good $\Sigma^+ \rightarrow p\ \pi^0$ decays.

The data from the 10,500 channels of SSD's, PWC's, and TRD's were read from the digital latches into buffer memories. The average event was 600 bytes long and took 600 μs to read out. Approximately 15,000 events were read out in each 23 s spill at 50% dead time. A processor farm analyzed 10% of the data online for monitoring purposes.

About 221 million triggers were recorded on magnetic tape during one month in the Fermilab 1990 fixed target running period. These data were taken with equal and opposite horizontal targeting angles near 3.7 mrad giving equal subsamples with the Σ^+ polarization up and down.

IV. DATA REDUCTION

A. Offline Reconstruction

The hits in each station of SSD and PWC were used to calculate the position of the track. Then particle trajectories were identified by finding events where the positions of the particle in the various stations made a straight line in the non-bend plane. Events were required to have exactly one charged track in each spectrometer. The momenta of the tracks were then fit. The vertex of the decay (Z_V), laboratory angle between hyperon and baryon (ϑ), and ratio of baryon momentum to hyperon momentum (R) were calculated. Undecayed beam events, characterized by ϑ near zero and R near unity, were rejected. Successfully reconstructed events with their fitted kinematic parameters were stored for further analysis. One-fiftieth of this sample was written to a special subsample (PRE) for ease in analysis of the high-statistics, low-background $\Sigma^+ \to p\ \pi^0$ decay.

The candidate decay events were analyzed under the hypothesis $\Sigma^+ \to p\ X^0$, calculating the missing mass squared ($M^2_{X^0}$) of the neutral (X^0). We formed the main data set for analysis with the following selection criteria: (1) hyperon momentum between 325 and 425 GeV/c, (2) decay vertex in the 12 m decay volume downstream of SSD 3, (3) reduced $\chi^2 \leq 4$ in the hyperon spectrometer and ≤ 2 in the baryon spectrometer. The large majority of the 48.6 million events in this main data set that satisfied these selection criteria were decays of $\Sigma^+ \to p\ \pi^0$, but a small peak of $\Sigma^+ \to p\ \gamma$ at $M^2_{X^0}=0\ GeV^2/c^4$ and a small shoulder of

$K^+ \to \pi^+\pi^0$ misanalyzed as Σ^+ are also visible (Figure 5). The 3.2×10^6 events in the $\Sigma^+ \to p\,\gamma$ region shown, ($-0.01 < M^2_{X^0} < 0.01$) were directed to a separate output stream. From these subsamples we formed data summary tapes (DST's) containing only fit results and a summary of the photon information. All further analysis for both asymmetry and branching ratio was done from these DST's.

In the analysis of both the asymmetry and branching ratio, further selections were made to isolate the signal. Events that had a missing neutral mass within 2 σ of the decay hypothesis $K^+ \to \pi^+\,\pi^0$ were rejected. These formed a 5% background in the radiative decay sample and 0.5% in the hadronic sample. Also, in both analyses, we required 70% of the total energy in the lead glass to be within 5 cm of the extrapolated neutral track, as described in section IV. B.

We found there was a class of hyperon tracks which did not project back to the hyperon production target. Although it was actually possible to include the narrow target in the fit to reject these events, we chose instead to select events based on the extrapolated position of the track at the target, since this did not depend on the absolute target position and could be more reliably simulated. Both the branching ratio and asymmetry analysis followed the strategy of examining the distribution of track positions at the production target and rejecting all events which were a given number of standard deviations away from the target in either transverse direction. The typical standard deviation of the distribution was 0.05 cm. For the asymmetry analysis we accepted events within ± 0.25 cm of the target position in X and ± 0.12 cm in Y. For the branching ratio we took events at ± 0.15 cm in both directions.

B. The TRD algorithm to separate γ and π^0

This algorithm tested the hypothesis that the missing neutral was a single photon. The position of the missing neutral (X^0) at the TRD was predicted from the fit hyperon and baryon tracks assuming only conservation of momentum ($Y \to B + X^0$). The resolution of this prediction was comparable to the position resolution of the TRD. In the case of a radiative decay ($X^0 = \gamma$) the extrapolated position was expected to coincide with the measured photon position. In the background decay ($X^0 = \pi^0$) the photons from π^0 had a finite opening angle and most of them deviated from the predicted direction of the π^0. The minimum opening angle of two gammas from the highest energy π^0 was 2 mrad, yielding a separation of 4 cm at the first TRD. The events displayed in Figure 6 illustrate the measurement of the position of the photon in the photon spectrometer. Figure 6A is an X projection of the charged particles in an electromagnetic shower as measured by the PWC and TRD. This event is interpreted as a shower produced by a single photon from Σ^+ radiative decay in the first steel converter. PWC wires that register signal are drawn as hits with single height. The PWC detects all charged particles in the shower and their hits are widely dispersed in space. The TRD is sensitive to the most forward high energy charged component of the electromagnetic shower and the TRD hits are grouped into the peak centered along the shower axis. The height of the TRD hit represents the number of pulses detected by the wire. Notice that the TRD is insensitive to the proton track but the PWC has hits associated with this track. Figure 6B shows a decay interpreted as $\Sigma^+ \rightarrow p\,\pi^0$. The two large clusters on either side of the predicted π^0 track are from the two photons.

The TRD algorithm calculated the position of the photon as the weighted average of the hit wires in the cluster. Clusters were defined as the set of consecutive wires with recorded signals between two wires with no signal. To choose the cluster for averaging, a quality factor was introduced as the sum of the square of the number of pulses on each wire in the cluster (see description of more details [69]). The largest cluster with a quality factor greater than 3 was used for coordinate calculation. If there was no cluster with quality > 3, we used the cluster which was the nearest one to the prediction.

The corresponding TRD χ^2 was formed by summing the square of the error-normalized distances between the extrapolated neutral track and the photon position determined by the TRD. The normalizing error included contributions from both TRD and extrapolation resolutions. For showers initiating in the first steel converter we used only the first pair of TRD to calculate χ^2, and only the second pair for showers in the second converter. Typically this TRD χ^2 distribution had 2 degrees of freedom for a single photon. We show the reduced TRD χ^2 in all plots and use it in all selections. Figure 7 shows the TRD χ^2 distribution for the decay $\Sigma^+ \rightarrow p\ \pi^0$ region around $M^2_{X^0} = m^2_{\pi^0}$ (dashed) and for the events with $-0.004 \leq M^2_{X^0} \leq 0.004$ (solid).

The further reduction of the π^0 background was done with the help of the photon calorimeter. The event displays in Figure 6 present the response of lead glass blocks in the measurement of the energy of photons. For events in the signal sample (but not for the events in the hadronic PRE sample), we required that at least 70% of the energy deposited in the photon calorimeter be within 5 cm of the extrapolated neutral track (local energy fraction). This rejects no signal and rejects a factor of two in background. By measuring the ratio of the energy within 5 cm of the track to the total energy measured by the calorimeter, we are less sensitive to the uncertainties in the energy scale of the photon calorimeter.

V. ANALYSIS AND RESULTS

A. Asymmetry Analysis

1. Signal isolation and extraction

After the above selections, we obtain the distribution of $M^2_{X^0}$ versus TRD χ^2 shown in Figure 8B. There is a clear excess of events near the photon mass for the region TRD $\chi^2 <$ 1.0. Figure 8A shows the $M^2_{X^0}$ distribution for events with TRD $\chi^2 < 1.0$ and events with TRD $\chi^2 > 4.0$. The events at large TRD χ^2 describe well the hadronic background under the radiative decay events. Four regions are shown in Figure 8B; signal (S) and background (B) in the region $\mid M^2_{X^0} \mid < 0.004\ GeV^2/c^4$, and two corresponding normalization regions (N and T). The fraction and number of radiative decay events in the signal region are f=1 $- N_B N_T / N_N N_S = 0.8315 \pm 0.0016$ and $f N_S = 34754 \pm 212$ events respectively where each N is the number of events in the corresponding region. The sample defined by these selections contains 52% of the estimated 67000 radiative decays which were reconstructed (Figure 5), and has a relatively small contribution from background (17%). The asymmetry of this background is measured by analyzing events in the background region.

2. Asymmetry calculation

We now proceed to analyze the asymmetries in the S and B regions as well as the hadronic sample (PRE). The angular distribution of the decay proton in the rest frame of the decaying Σ^+ is given by (7).

$$\frac{dN}{d\Omega} = \frac{N_0}{4\pi}(1 + \alpha \mathbf{P} \cdot \hat{\mathbf{n}}) \tag{7}$$

The asymmetry vector $\mathbf{A} = \alpha \mathbf{P}$ is the asymmetry parameter times the polarization vector. The total number of events in the given sample is N_0. We choose the unit vectors of $\hat{\mathbf{y}}$ in the vertical direction, $\hat{\mathbf{z}}$ in the direction of the beam, and $\hat{\mathbf{x}}$ to form a right-handed coordinate system. Integrating over the azimuth in each case, we obtain (8) where ϵ_{ij} is the efficiency for observing an event including geometrical acceptance, trigger efficiency, and reconstruction efficiency. The efficiency depends on θ_j, the angle in the center of mass frame between the j direction and the outgoing proton, and Θ_X, Θ_Y, which are the horizontal and vertical angles respectively of the hyperon, measured in the lab. The index i (suppressed in equations (9)-(13)) labels a specific sample, and j labels the direction.

$$\frac{2}{N_{0i}} \frac{dN}{d\cos\theta_j} = \epsilon_{ij}(\cos\theta_j, \Theta_X, \Theta_Y)(1 + A_{ij}\cos\theta_j)_{j=X,Y,Z}^{i=\pi^0,S,B,\gamma} \tag{8}$$

If the efficiency were known we could measure the asymmetry vector $\mathbf{A} = \alpha \mathbf{P}$ directly. Instead we choose to cancel the efficiency by comparing data from two targeting angles with polarizations of opposite signs and approximately equal magnitudes. Let N^+ and N^- represent the normalized cosine distributions as in (8) for positive and negative targeting angle respectively. In the limit that ϵ and $\mid \mathbf{A} \mid$ are the same for both targeting angles we have:

$$\frac{N^+ - N^-}{N^+ + N^-} = A_j \cos\theta_j \tag{9}$$

Parity conservation of the strong interaction allows polarization only in the Y direction, perpendicular to the X-Z scattering plane. If the cosine distributions in the other two directions are not the same, this is a sign of efficiency effects. The raw cosine distributions are shown in Figure 9A-C for the hadronic region and Figure 10A-C for the signal regions. In part B of Figures 9 and 10 we see the effects of the asymmetry that we are trying to measure, with the sign of the slope changing between the two targeting angles. Part C shows the clear dip near −0.4 which results from the kinematic rejection of events consistent with $K^+ \rightarrow \pi^+ \pi^0$.

Examination of the cosine distributions in the X direction shows that the efficiencies are not the same (Figure 9A). Figure 11 shows that the beams of the two targeting angles have different distributions of horizontal angles (Θ_X). If we take a restricted range of Θ_X, shown on Figure 11A, we obtain cosine distributions where the two targeting angles are very similar (Figure 11B). So although the overall efficiency for the two beam phase spaces is not the same, it is possible to have the efficiencies for a given Θ_X,Θ_Y be equal for the respective samples and calculate asymmetry in a set of these bins. For Θ_X we used eight bins and for Θ_Y we used two. In addition, $\cos\theta_j$ is also divided into 15 bins.

For each of the 16 (Θ_X), (Θ_Y) bins k, in each of three directions j we have a measurement $A_{jkl}\cos\theta_{jl}$ in each of fifteen cosine bins l. We fit these fifteen measurements for a slope A_{jk}, constraining the intercept to be zero. The weighted fit is formally given by (10)

$$A_{jk} = \frac{\sum_{lm} \cos\theta_{jm} W_{lm} (A_{jkl}\cos\theta_{jl})}{\sum_{lm} \cos\theta_{jm} W_{lm} \cos\theta_{jl}} \tag{10}$$

and the error is given by (11)

$$\sigma_{A_{jk}} = (\sum_{lm} \cos\theta_{jm} W_{lm} \cos\theta_{jl})^{-\frac{1}{2}} \tag{11}$$

The A_{jkl} are slightly correlated with a covariance matrix given by (12)

$$W_{lm}^{-1} = \sigma_{lm}^2 = \frac{(1-(A_{jkl}\cos\theta_{jl})^2)(1-(A_{jkm}\cos\theta_{jm})^2)}{4}[\delta_{lm}(\frac{1}{N_{jkl}^+} + \frac{1}{N_{jkl}^-}) - (\frac{1}{N_{0jk}^+} + \frac{1}{N_{0jk}^-})] \tag{12}$$

Ignoring the small and negative off-diagonal terms, we obtain

$$W_{ll}^{-1} = \sigma_{ll}^2 = \frac{(1-(A_{jkl}\cos\theta_{jl})^2)^2}{4}\left(\frac{1}{N_{jkl}^+} + \frac{1}{N_{jkl}^-}\right) \tag{13}$$

Then we average the A_{jk} over the 16 (Θ_X), (Θ_Y) bins to get the asymmetry, A_j. In this way we can extract the asymmetry directly from the data. We refer to this method as our bias canceling procedure. No Monte Carlo simulation of the efficiency was required or used in this analysis.

Figures 9D-F and 10D-F show $\mathbf{A}_j \cos\theta_j$ as a function of $\cos\theta_j$. To calculate these distributions we use equation (9) with N^- as the spin down +3.7 mrad sample (POS) and N^+ as the spin up -3.7 mrad sample (NEG). The dashed symbols indicate this ratio before the bias canceling procedure is applied, and the solid symbols show the same ratio afterwards. It is seen clearly that the false asymmetry in the X direction is removed completely by this method.

3. Measured asymmetries

When the bias canceling procedure is applied to the signal and background (S and B) regions, and the hadronic sample, we obtain the asymmetries in Table VI. The asymmetry of the radiative decay events is extracted by taking the asymmetry of the events in the signal region as a linear combination of radiative and background events with relative fraction f:

$$A_{SY} = fA_{\gamma Y} + (1-f)A_{BY} \tag{14}$$

TABLE VI. Asymmetry components for each sample. The quoted errors are statistical only. The Σ^+ polarization is along the Y direction so that A_X and A_Z should be zero.

Sample		A_X	A_Y	A_Z
Hadronic	π^0	-0.0050 ± 0.0021	-0.1188 ± 0.0021	-0.0011 ± 0.0021
Signal	S	$+0.0088 \pm 0.0082$	-0.0884 ± 0.0083	-0.0004 ± 0.0108
Background	B	$+0.0121 \pm 0.0073$	-0.0938 ± 0.0081	-0.0373 ± 0.0064
Radiative	γ	$+0.0082 \pm 0.0100$	-0.0873 ± 0.0102	$+0.0070 \pm 0.0130$

The asymmetry parameter for the radiative decay is then determined from the ratio of radiative to hadronic asymmetries multiplied by the known value for the hadronic asymmetry parameter.

$$\alpha_\gamma = \frac{A_{\gamma Y}}{A_{\pi^0 Y}} \alpha_{\pi^0} = \frac{\alpha_{\pi^0}}{f A_{\pi^0 Y}} [A_{SY} - (1-f) A_{BY}] \tag{15}$$

Using $f = 0.8315 \pm 0.0016$, the measured asymmetries from Table VI, and $\alpha_{\pi_0} = -0.980^{+0.017}_{-0.015}$ [5], we obtained

$\alpha_\gamma = -0.720 \pm 0.086$

where the error is statistical.

It should be noted that we are measuring a ratio of two asymmetries here and so any residual first-order errors in the asymmetry from polarization differences or acceptance differences will also be similar between the two decay modes and be diluted in the ratio.

By replacing N^+ and N^- in (12) with their $\cos\theta$ dependence from (8), and then approximating (11) with an integral and taking the limit of small A, we see that the statistical error of the asymmetry A = αP is approximately $\sqrt{3/N}$, where N is the total number of events in the sample. The error on α_γ varies inversely with polarization. In our experiment polarization was only 12%. However, the high statistics of the experiment allowed a statistical precision in α_γ of 0.086, better than in previous experiments with large polarization but with low statistics. More importantly, the high statistics also allowed us to divide up the data into many subsamples to ensure reliable control of the systematic errors.

4. Systematic errors

The Σ^+ is positively polarized, therefore the direction of Σ^+ polarization is in the $\pm$Y direction for negative and positive targeting angles respectively. Thus we would expect to see an asymmetry in the Y direction but not in the X and Z directions. All the X and Z asymmetry components are consistent with zero with the exception of A_{BZ}. It is not surprising that there is a residual bias in this component, because the background sample is dominated by incorrectly measured hadronic decays. Only the biases in the Z direction depend on the hyperon momentum measurement, which forms the largest class of measurement errors in our apparatus. We observed that A_{BZ} changed (but did not vanish) when we calculated the asymmetry using data in a restricted range of hyperon momentum, or using the average value of the asymmetry found in 2 bins of hyperon momentum. Although the value for A_{BZ} varied in these studies, the values of α_γ in the same studies varied by only 0.020 from the normal technique. We assign this variation as a systematic error to α_γ.

We estimated the systematic error due to the TRD algorithm by analyzing the data with several different algorithms. These included an early version of the algorithm which calculated χ^2 based on the nearest hit to the projected track in all eight planes [70]. Also an experimental algorithm was developed which required large clusters in the first X and Y TRD after the conversion point. Finally we ran the standard algorithm but selected only those events with extrapolation error of 3 cm or less. We estimate this systematic error to be equal to the largest deviation between these answers and the answer from the normal technique, 0.022.

The answer used the default binning of 15 $\cos\theta$ bins, 8 (Θ_X) bins, and 2 (Θ_Y) bins. To test the effects of binning, all combinations of 10, 15 and 30 $\cos\theta$ bins, 8 and 16 bins in (Θ_X), and 1, 2, 4, 8, and 16 bins in (Θ_Y) were generated. This yielded a distribution of 30 values for α_γ with a σ of 0.025. We take this to be the systematic error due to the binning variation.

We estimated the stability of the result by dividing the data within the final data sample into eight bins in each of 17 variables on which some selection had been made. In each of the eight bins we calculate α_γ, then calculate a χ^2 that the eight values of α_γ fit a constant. The distribution of these χ^2 with seven degrees of freedom has a mean of 7.50 ± 1.14. The reduced distribution of χ^2/ν has a mean of 1.07. This shows that, within the data region, the answer is stable with respect to the parameters we used to select the sample, and the statistical errors describe the error well. We estimate a limit on the systematic error by calculating what amount of error could be added in quadrature to the statistical error to cause the mean of the reduced χ^2 distribution to move from the most probable value of 1 to 1.07. This would be $\sqrt{0.07}$ the size of the statistical error, or 0.023. We take this as a conservative upper bound on the systematic error due to the sample selection.

The final systematic error is just the sum in quadrature of the four errors, shown in Table VII, ± 0.045.

The result is [13]

$$\alpha_\gamma = -0.720 \pm 0.086 \pm 0.045$$

where the first error is statistical and the second is systematic. This result is in agreement with the previous low statistics measurements and confirms with high statistics and with low systematic error that the asymmetry in Σ^+ radiative decay is indeed large and negative.

TABLE VII. The four contributions to the systematic error of α_γ

Source	Error
Background z false asymmetry	± 0.020
TRD Algorithms	± 0.022
Bias canceling technique	± 0.025
Data stability	± 0.023
Quadrature sum	± 0.045

B. Branching Ratio Analysis

The relative ratio is given by

$$\frac{BR(\Sigma^+ \to p\,\gamma)}{BR(\Sigma^+ \to p\,\pi^0)} = \frac{\frac{N_\gamma}{\epsilon_\gamma}}{\frac{N_\pi}{\epsilon_\pi}} \tag{16}$$

where N_π is the number of $\Sigma^+ \to p\,\pi^0$ and N_γ is the number of $\Sigma^+ \to p\,\gamma$ events, obtained from the data. The corresponding efficiencies for observing these decays ϵ_π and ϵ_γ are determined by a Monte Carlo simulation of the apparatus. When the TRD algorithm is used to isolate $\Sigma^+ \to p\,\gamma$ events, ϵ_γ is multiplied by ϵ_{TRD}, the efficiency of that algorithm which we measure from the data. Since we are measuring a ratio, we use similar selections on the samples which contain radiative and hadronic decays, in order to maximize the cancellation of common errors. The positive (POS) and negative (NEG) targeting angle data were kept separate throughout the analysis because of their different beam phase spaces, requiring a separate Monte Carlo simulation for each.

In addition to the selections made in Section IV. A, all events which were triggered only by the rear lead glass were rejected. Decays in the first meter of the decay volume were rejected to reduce interaction background. Events were required to have angle $\vartheta > 0.3$ mrad, and ratio of baryon to hyperon momentum $R < 0.98$. The decay protons were required to be well inside the hole in the photon calorimeter.

1. Number of $\Sigma^+ \to p\,\pi^0$

After all the selections are applied to the hadronic PRE sample, there is still a small background remaining in the data for $\Sigma^+ \to p\,\pi^0$ (Figure 12A). The Monte Carlo simulation of $\Sigma^+ \to p\,\pi^0$ decays (Figure 12B) shows some non-Gaussian tails but not at the level that are seen in the data. Some $\Sigma^+ \to p\,\gamma$ are visible in Figure 12A; we estimate 500 based on the results of the next section. The rest of the background is composed of mismeasured $\Sigma^+ \to p\,\pi^0$ and beam interactions. The peak is fit with the sum of two Gaussians plus a first degree polynomial, shown as the solid line on Figure 12A, and the polynomial parameters are used to estimate the size of the background, shown as the dashed line on Figure 12A.

The number of $\Sigma^+ \rightarrow p\ \pi^0$ in the PRE sample is determined by taking the total number of events on the mass plot from $M^2_{X^0} = -0.02$ to $0.06\ GeV^2/c^4$, and subtracting the 500 estimated $\Sigma^+ \rightarrow p\ \gamma$ and the number of events in the background. We assign a statistical counting error equal to the square root of the number of $\Sigma^+ \rightarrow p\ \pi^0$ found, and take the number of events in the background as an upper bound on the systematic error of this number, thus allowing for the possibility that all the background is $\Sigma^+ \rightarrow p\ \pi^0$ or that the linear fit underestimates the background. The results are shown in Table VIII. Since the PRE sample is 2% of the data, the number obtained is $N_\pi/50$ and the number is multiplied by 50 for use in calculating the final result.

TABLE VIII. Number of $\Sigma^+ \rightarrow p\ \pi^0$in analyzed PRE sample ($N_\pi/50$)

Targeting Angle	Number	Stat. Error	Syst. Error
POS	267415	517	2908
NEG	246222	496	2478

2. Number of $\Sigma^+ \rightarrow p\ \gamma$

To determine the number of $\Sigma^+ \rightarrow p\ \gamma$, N_γ, in the branching ratio formula (16), we made an additional selection on the signal sample, requiring the predicted position of the neutral track to be within the steel converter, at least 5 cm from the outside edges and 3 cm from the converter hole in X and Y. This allowed us to avoid making corrections on the inefficiency in triggering of showers at the edges of the calorimeter and near the hole. Then we proceeded to fit two samples to determine the number of radiative decays: (1) all the events passing the above selections, and (2) those events with TRD $\chi^2 < 10$. Requiring TRD $\chi^2 < 10$ reduces the background by a factor of 2.9, so the separate results from these two samples provide a check of the stability of our result with varying backgrounds.

The statistics of the signal are large enough to illuminate the non-Gaussian behavior of the resolution of the apparatus and the nonlinear dependence of $M^2_{X^0}$ on ϑ and hyperon and baryon momenta. Therefore a fitting procedure in which we know the resolution function of the apparatus is necessary. Instead of using a Monte Carlo simulated resolution function, we used experimental information from the peak of the $\Sigma^+ \rightarrow p\ \pi^0$ decay. In each targeting angle we fit the entire sample of $\Sigma^+ \rightarrow p\ \pi^0$ from the main data set (see Sec. IV. A) as the sum of two Gaussians, obtaining H, X_M, and σ, the amplitude, center, and width (as standard deviation) of each Gaussian respectively. (The centers are close enough that we report and use only the center of the larger Gaussian.) From these results, shown in Table IX, we can calculate F, the relative fraction of each Gaussian present, using (17).

$$F_1 = \frac{H_1\sigma_1}{H_1\sigma_1 + H_2\sigma_2} = 1 - F_2 \qquad (17)$$

TABLE IX. Resolution function parametrizations

Sample	H_1	H_2	X_M	σ_1	σ_2	F_1
	Events/0.0001GeV^2/c^4		GeV^2/c^4	GeV^2/c^4	GeV^2/c^4	
POS	253556	86070	0.01787	0.00217	0.00435	.595
NEG	246660	88400	0.01792	0.00219	0.00437	.583

Figure 13 shows the resolution function from positive targeting angle data fit to all the events from the positive targeting angle in the main data set defined in section IV. A. Although this even function cannot duplicate the asymmetry of that peak, it does reproduce the integral precisely.

We then fix relative fractions of the two Gaussians, (F_1, F_2) and fit the function (18) to the $\Sigma^+ \rightarrow p\ \gamma$ data sample with the total number of events N, the combined center X_M, and the scaling factor W which scales the widths σ_1 and σ_2 in order to translate the resolution function from the π^0 mass squared to the γ mass squared, and determine the number of radiative decays N.

$$RES(x; N, X_M, W) = \frac{N}{\sqrt{2\pi}}\left(\frac{F_1}{\sigma_1 W}\exp\left(-\frac{(x - X_M)^2}{2(\sigma_1 W)^2}\right) + \frac{F_2}{\sigma_2 W}\exp\left(-\frac{(x - X_M)^2}{2(\sigma_2 W)^2}\right)\right) \tag{18}$$

The $\Sigma^+ \rightarrow p\ \gamma$ data is fit with the form $RES(x; N, X_M, W) + exp(a + bx) + c + dx$, parametrizing the background by linear and exponential contributions with free parameters. The errors are supplied by the MINOS function of the CERN MINUIT package [71], and are generally asymmetric. The values obtained in the fit to the $\Sigma^+ \rightarrow p\ \gamma$ sample are shown in Table X, and shown in Figure 14 superimposed on the data. The dashed line indicates the contribution of the fitted background. The results are summarized in Table XI.

TABLE X. Parameters from fits to $\Sigma^+ \to p\,\gamma$ data

Sample	N_γ	$X_M(GeV^2/c^4)$	W	a	b	c	d	χ^2/ν
POS All Data	19500	−0.00047	1.08	2.33	610	127	4837	1.03
NEG All Data	18708	−0.00046	1.09	3.10	549	118	4222	1.08
POS TRD < 10	16411	−0.00046	1.09	1.85	556	−1.08	−1077	1.09
NEG TRD < 10	15490	−0.00047	1.10	2.35	527	10.94	−289	1.10

TABLE XI. Number of $\Sigma^+ \to p\,\gamma$

Targeting Angle	Number	−Stat. Error	+Stat. Error
POS All data	19500	1281	1402
NEG All data	18708	1581	1660
POS TRD < 10	16411	961	1064
NEG TRD < 10	15490	1178	1219

3. Efficiency of TRD algorithm:

The efficiency of the TRD algorithm for correctly identifying single photons was measured from data with a separate sample of single photons. We used a sample of $\Sigma^+ \rightarrow p\ \pi^0$ in which one photon converted in the steel and was measured in the main lead glass array and the other photon went into the hole of the calorimeter and was measured in the rear lead glass. Some of these photons showered in an X chamber frame of the downstream PWC D proportional chambers, and the position of the resultant electromagnetic shower was measured in the last two planes (U and V) of that station. With a position measurement of the photon that showered downstream and the momentum vector and vertex of the π^0 obtained from the charged track information, it was possible to predict the trajectory of the other photon. Using this predicted trajectory we calculated the χ^2 with the hits in the TRD as described in section IV.B. The χ^2 distribution is shown in Figure 15A, and the efficiency of the TRD algorithm vs. χ^2 is shown in Figure 15B. We observe a plateau in the efficiency above χ^2 of 10, and choose to keep all events with $\chi^2 < 10$, thus avoiding the area where the efficiency is changing rapidly. With this selection the differences in the χ^2 distribution at low χ^2 between true $\Sigma^+ \rightarrow p\ \gamma$ events and these events do not affect our efficiency. Since 35% of $\Sigma^+ \rightarrow p\ \pi^0$ events also have a $\chi^2 < 10$, the background rejection is 2.9:1.

Table XII shows the results of the TRD efficiency for both targeting angles. Recall that the probability that the photon converts in the steel is only 0.909. The statistical error is assigned from the binomial distribution based on the sample size of 3825 events in positive and 4244 events in negative targeting angle. By examining the variation of the efficiency across the TRD in space, we assign a systematic error to the efficiency. We see evidence for systematic shifts only in the negative targeting angle. We set an upper bound on possible systematic errors of the positive targeting angle efficiency by calculating the smallest systematic error to which our technique would have been sensitive.

TABLE XII. Efficiency of TRD at $\chi^2 < 10$

Targeting angle	Efficiency	Stat. Error	Syst. Error
POS	0.8260	0.0061	**0.0046**
NEG	0.8320	0.0057	**0.0047**

4. Simulation of the experimental efficiencies

A detailed Monte Carlo simulation of the experimental apparatus was performed to compute the detection efficiencies of the decays $\Sigma^+ \rightarrow p\ \gamma$ and $\Sigma^+ \rightarrow p\ \pi^0$ which are needed for calculation of the branching ratio for these decays. The Monte Carlo was based on the GEANT code, version 3.14 [72]. About 100,000 decays of each decay mode were generated isotropically in their center-of-mass systems at both positive and negative targeting angles. The experimental beam phase space (measured momentum, horizontal and vertical angles, the X,Y coordinates of beam particles) was directly used in the simulation of the phase space for Σ^+ before their decays. This information was available as the results of the analysis of $T1_{P_r}$ beam triggers. The charged particles, Σ^+ and protons from Σ^+ decays, were subject to Moliere multiple Coulomb scattering in the material of the hyperon and baryon spectrometers during their passage through the apparatus. The hits of charged particles within geometrical acceptances of all coordinate detectors of hyperon and baryon spectrometers were digitized with 100% efficiency and recorded on disk in the same format as the data. They were further analyzed by the same offline code and with the same selection as the data. Figure 12 shows the comparison of missing mass squared distributions $[M^2_{X^0}]$ for data and simulated events for the decay $\Sigma^+ \rightarrow p\ \pi^0$. The fit to the data in (A) described in section V.B.1 is scaled and superimposed as the dashed line on the simulated events (B).

The hyperon decays were generated so they would all take place in a region of decay vertex Z_V ranging from 0.0 m (the upstream end of the decay volume) to 14.0 m, which is longer than the region of Z_V bounded by the offline analysis selections, $+1.0\ \text{m} < Z_V < 12.0\ \text{m}$. The simulation was checked to ensure that the ratio of radiative to hadronic decays satisfying T3 trigger did not change if we restricted the allowed region of decays to $1.0\ \text{m} < Z_V < 12.0\ \text{m}$.

The simulation set indicators within the simulated events to indicate whether or not the various requirements of the trigger and the trigger itself were satisfied. The showers produced by photons in the steel converters of the photon spectrometer were generated with a cutoff at 100 MeV below which secondary particles were not propagated, to save computing time during the simulation process. The variation of this threshold did not change the efficiency of the T2 trigger. The requirements for the T3 trigger component E(all) > 5 GeV were simulated with a simplified approach. This approach counted only the energies of photons and secondary particles whose momentum directions pointed into the geometrical acceptance region of the photon calorimeter. No showers were simulated in the calorimeter and no energy leakage or resolution effects in the calorimeter were included in the simulation of the T3 trigger. However, the selections we have applied, including requiring the photon to point at least 3 cm away from the hole, and an opening angle of at least 300 μrad, effectively require that the photon energy is at least 20 GeV, well above the trigger threshold of 5 GeV.

There is a significant probability that the photon from the radiative decay of Σ^+ converts into an e^+e^- pair in the media between the decay vertex and the first veto counter, V1, of the photon spectrometer. These particles can fire the V1 counter and veto the T2 trigger. This happens twice as often for $\Sigma^+ \rightarrow p\ \pi^0$ decays due to the decay $\pi^0 \rightarrow \gamma\gamma$. This process was included in the simulation, decreasing the initial T2 efficiency.

By isolating a sample of $\Sigma^+ \rightarrow p\ \pi^0$ from minimum bias triggers ($T1_{P_r}$), we see that some $\Sigma^+ \rightarrow p\ \pi^0$ events do not satisfy the T2 trigger requirements. In these events, secondary interactions of protons from Σ^+decay or muons in random coincidence make a signal in the V1 or V2 counters and cause the event to be vetoed. The inefficiency due to these processes is 12.2% for positive targeting and 10.8% for negative targeting angle. This part of the T2 inefficiency is the same for both decay modes and is cancelled in the ratio of efficiencies for radiative and hadron decay modes.

The total efficiencies are the result of geometrical acceptance, track finding efficiencies, software selection and T3 trigger requirements. They are presented in Table XIII for 100000 simulated $\Sigma^+ \rightarrow p\ \pi^0$ and $\Sigma^+ \rightarrow p\ \gamma$ decays at each targeting angle.

TABLE XIII. Monte Carlo efficiencies of detection of $\Sigma^+ \rightarrow p\,\pi^0$ and $\Sigma^+ \rightarrow p\,\gamma$ decays and their ratio. * denotes efficiencies used in BR calculation.

	π^0		γ		π^0/γ	
	Pos	Neg	Pos	Neg	Pos	Neg
After trackfinding	0.780	0.756	0.747	0.720	1.044	1.051
After selections	0.358	0.290	0.356	0.292	1.006	0.995
T3 Trigger	0.299	0.244	0.247	0.207	1.211	1.179
T3 with hole selection +3 cm			0.189	0.158	1.584	1.549
Corrected for Dalitz decay	*0.296	*0.242	*0.189	*0.158	1.566	1.554

The efficiencies are significantly different at positive and negative targeting angles due to different corresponding beam phase spaces; however the ratio of efficiencies is much less sensitive to them. We note with * the efficiencies which were used in computing of the branching ratio.

The simulation of $\Sigma^+ \rightarrow p\ \pi^0$ assumed the π^0 would decay to $\gamma\gamma$. In fact 1.198% of them decay via the Dalitz decay $\pi^0 \rightarrow e^+e^-\gamma$. We calculate that 90 ± 10% of these events will be rejected in the veto counters, thus contributing to the systematic uncertainty. Thus the efficiency obtained for $\Sigma^+ \rightarrow p\ \pi^0$ by the simulation of these decays is multiplied by a correction factor of .9892 ± .0012 in the final answer.

5. Systematic errors

The ratios N_π/ϵ_π and N_γ/ϵ_γ represent the initial number of the corresponding decays. As given by 16, their ratio is the ratio of branching ratios. High statistics allowed us to check the stability of the initial numbers of decays by dividing the data into subsamples and measuring the ratios in each subsample.

The quality of the MC reproducing the data can be explored by dividing the phase space into subsamples and measuring the ratio N_π/ϵ_π and N_γ/ϵ_γ in each subsample. In each of fourteen variables, we divided the data into five equal-statistics slices based on the distribution of the Monte Carlo events. This gave the opportunity to test our fitting techniques in regions of varying kinematics and varying signal-to-background ratio. The coordinates which we measured were: X, Y, p, Θ_X, Θ_Y of the hyperon, X, Y, and p of the baryon, predicted Y position of photon at the TRD, center-of-mass decay angle $\cos\theta_y$, R=p_B/p_Y, ϑ, Z_V, and the distance of the predicted photon position from the hole.

In the $\Sigma^+ \rightarrow p\ \pi^0$ case, this technique is sensitive enough to see the expected effects. For instance, comparing polarized data against unpolarized Monte Carlo simulation one ought to see a linear trend in the five slices of $\cos\theta_Y$, and in fact there is such a trend. But this technique will also identify regions of phase space where the Monte Carlo does not reproduce the data well. The effects are quantified by forming a χ^2 that all five values fit a constant. Thus fourteen χ^2 are obtained, and when reduced they should themselves form a reduced χ^2 distribution with four degrees of freedom. Large deviations of the mean from unity show errors that are not quantified by the statistical error.

We test the significance of the deviation of the mean from unity by calculating the standard error of the mean from the theoretical width of the reduced χ^2 distribution, and requiring for a significant systematic error that the mean of the distribution be more than one standard error larger than unity. This corresponds to the 80% confidence level that this enlarged mean did not occur by chance. If the mean is consistent with or less than unity, we set a upper limit based on the smallest systematic error that this technique has the sensitivity to detect, namely a mean greater than unity by just 1 standard error. All of the χ^2 distributions in the branching ratio have means that are significantly greater than unity except for the case of the POS ALL TRD sample, where we set a limit.

We find in the case of $\Sigma^+ \rightarrow p\ \pi^0$ a relative error of 3.96% for positive targeting angle and 4.39% for negative. This is added in quadrature with the systematic error on the background subtraction for $\Sigma^+ \rightarrow p\ \pi^0$ to obtain the systematic error on the ratio.

For $\Sigma^+ \rightarrow p\ \gamma$ this process also quantifies the errors which may be made by our fitting procedure in regions of extreme resolution or signal/background variation. We do the study independently for a data sample with TRD $\chi^2 < 10$ and for all the data. In some bins no signal is visible due to the large amount of background, in these cases two bins are combined to get enough signal to fit. The same is done where the background obviously does not fit the form above.

A summary of the contributions (in percent) to the systematic error is given in Table XIV. The systematic errors for efficiency of the TRD algorithm were presented earlier. The total relative systematic error was calculated as a sum in quadrature of independent contributions.

TABLE XIV. Contributions to relative systematic error (in %)

Sample	N_π/ϵ_π	N_γ/ϵ_γ	TRD	Total syst. error	Stat. error
POS All Data	4.10	3.21		5.21	7.24
NEG All Data	4.50	4.14		6.12	8.92
POS TRD $<$ 10	4.10	3.42	0.56	5.37	6.58
NEG TRD $<$ 10	4.50	4.76	0.57	6.58	7.96

6. Averaging and final result

When averaging the results from the positive and negative targeting angles together, we note that they are essentially independent measurements. Thus their systematic errors, which were measured independently, are assumed to be uncorrelated. We follow the Particle Data Group method [5] of averaging two measurements with asymmetric error bars. This gives an answer with a symmetric total error. We can unfold the statistical and systematic errors in the total error by performing the whole averaging process using statistical errors only, thus finding the statistical error of the average, and use it to extract the systematic error of the average from the total error.

The answers obtained with and without the TRD selection are consistent within errors of each other, and just slightly different in the amount of total error; we obtain only 0.03% less total error by using the TRD. Thus by two independent analysis methods in which signal to background varies by a factor of 2.9, we have essentially the same answer. Table XV summarizes the numbers used to arrive at the answer. The results from each sample as well as the averages of each method are shown in Table XVI. We choose the result that uses the TRD because the overall error is slightly smaller, the background is smaller, and the smaller statistical error gives us more sensitivity to the systematic errors.

The relative branching ratio BR $(\Sigma^+ \rightarrow p\,\gamma/\Sigma^+ \rightarrow p\,\pi^0)$ which we have measured in our experiment with a sample of 31901 events is

$$\mathrm{BR}\,(\Sigma^+ \rightarrow p\,\gamma/\Sigma^+ \rightarrow p\,\pi^0) = (2.32 \pm\ 0.11 \pm\ 0.10) \times 10^{-3}$$

where the first error is statistical and the second error is systematic. When we multiply the relative branching ratio times the absolute branching ratio for $\Sigma^+ \rightarrow p\,\pi^0$ [5], 0.5157, we obtain an absolute branching ratio for $\Sigma^+ \rightarrow p\,\gamma$ for comparison purposes, shown in Table XVII.

TABLE XV. Values used for the calculation of BR ($\Sigma^+ \to p\,\gamma / \Sigma^+ \to p\,\pi^0$)

	POS All Data	NEG All Data	POS TRD<10	NEG TRD<10
N_γ	19500^{+1402}_{-1281}	18708^{+1660}_{-1581}	16411^{+1064}_{-961}	15490^{+1219}_{-1178}
$N_\pi/50$	267415 ± 517	246222 ± 496	267415 ± 517	246222 ± 496
ϵ_γ	0.189 ± 0.0012	0.158±0.0011	0.189 ± 0.0012	0.158±0.0011
ϵ_π	0.296±0.0014	0.242±0.0013	0.296±0.0014	0.242±0.0013
ϵ_{TRD}			0.826±0.0061	0.832±0.0057

TABLE XVI. Results of Relative BR ($\Sigma^+ \to p\,\gamma / \Sigma^+ \to p\,\pi^0$) in units of 10^{-3}

Sample	Relative BR	-Stat	+Stat	Syst
POS TRD < 10	2.329	0.139	0.153	0.125
NEG TRD < 10	2.317	0.178	0.184	0.153
AVERAGE TRD < 10	2.324	0.113	0.113	0.097
POS All Data	2.287	0.151	0.166	0.119
NEG All Data	2.330	0.198	0.208	0.143
AVERAGE All Data	2.304	0.125	0.125	0.092

TABLE XVII. Comparison with previous world average branching ratio in units of 10^{-3}

	Ratio	Total error
E761 BR($\Sigma^+ \to p\,\gamma / \Sigma^+ \to p\,\pi^0$)	2.324	0.149
E761 BR($\Sigma^+ \to p\,\gamma$)	1.20	0.08
Prev. World Average [5]	1.25	0.07

VI. CONCLUSIONS

This experiment confirms, with higher statistical precision and well-understood systematics, the results of previous measurements of $\Sigma^+ \to p\,\gamma$. We have shown that the asymmetry parameter in this decay mode is large and negative and that it cannot be due to background contamination from the $\Sigma^+ \to p\,\pi^0$ decay with its large and negative asymmetry parameter. Also, our experiment provided the most precise data on the rate of the $\Sigma^+ \to p\,\gamma$ decay, confirming that the rate is not inflated by contribution from background.

Our measurement of the $\Sigma^+ \to p\,\gamma$ rate together with our previously published measurements of the rates of $\Xi^- \to \Sigma^-\,\gamma$ [11] and $\Omega^- \to \Xi^-\,\gamma$ [12] allows us to make observations about the hierarchy of the hyperon radiative decay rates. We note that the rates of radiative decay are much higher when the initial hyperon contains a valence u quark, specifically in the decays $\Sigma^+ \to p\,\gamma$, $\Xi^0 \to \Sigma^0\,\gamma$, $\Xi^0 \to \Lambda\,\gamma$, and $\Lambda \to n\,\gamma$. This may be due to the possibility of interquark W-exchange (Figure 1C), for which a valence u quark is required. The $\Sigma^+ \to p\,\gamma$ rate considerably exceeds the unitarity limit. In contrast, the rate for $\Xi^- \to \Sigma^-\,\gamma$ is consistent with the unitarity lower bound. The Ξ^- has no valence u quark so the internal W-exchange is forbidden. In the $\Omega^- \to \Xi^-\,\gamma$ decay W-exchange should also be forbidden and the experimental data [12] seem to support this conclusion. So the theory of the weak radiative decays should take into account this difference.

Definitely the most striking feature of the $\Sigma^+ \to p\,\gamma$ decay is the observed very large and negative asymmetry parameter in contradiction with the prediction of Hara's theorem that the asymmetry parameter is zero. This theorem is based on flavor SU(3) symmetry, and its failure to reproduce the asymmetry of the $\Sigma^+ \to p\,\gamma$ decay means that the SU(3) symmetry is essentially violated in this decay. Now the challenge for theory is to explain the mechanism of the SU(3) symmetry violation. The QCD sum-rules approach [52] is a microscopic approach which has obtained values for the $\Sigma^+ \to p\,\gamma$ rate and asymmetry parameter consistent with experiment. Unfortunately, this approach includes summation over many diagrams, and therefore the reliability is not so evident. It is important to extend the comparison of the theory and experiment to some other radiative decays.

One good candidate for such a future comparison might be the $\Xi^- \to \Sigma^- \gamma$ decay. Our experience shows [11] that in principle, measurement of the asymmetry parameter is possible for this decay. Hara's theorem predicted that the $\Xi^- \to \Sigma^- \gamma$ asymmetry parameter would also vanish in the limit of SU(3) symmetry [1]. This decay appears similar to $\Sigma^+ \to p\, \gamma$ on the hadronic level since they both connect two members of a U-spin doublet, but on the quark level they are fundamentally different because internal W-exchange is forbidden for Ξ^-. Hara's theorem does not directly address the as yet unmeasured asymmetry parameter of $\Lambda \to n\, \gamma$. However, this asymmetry parameter can also give valuable information because like the Σ^+ it has a valence u quark but on the hadronic level it transforms differently under U-spin. These future measurements have the potential to determine whether or not the same mechanism of SU(3) breaking is working in each radiative decay. The knowledge we are learning on the quark level could then be applied to better determine the applicability and limits of flavor SU(3) symmetry.

ACKNOWLEDGEMENTS

We wish to thank the staffs of Fermilab and the Petersburg Nuclear Physics Institute for their assistance. The loan of the photon calorimeter lead glass from Rutgers University is gratefully acknowledged. The BGO crystals were produced by the Shanghai Institute of Ceramics, Academica Sinica, Shanghai, People's Republic Of China. We thank Ya. Azimov of the Petersburg Nuclear Physics Institute for helpful discussions of the theory. This work is supported in part by the U.S. Department of Energy under contracts DE-AC02-76CH03000, DE-AC02-76ER03075, and grants DE-FG02-91ER40682, DE-FG02-91ER40664, and DE-FG02-91ER40631, the Russian Academy of Sciences, the Chinese National Natural Science Fund (DE-19075049 and DE-19375041), and the UK Science and Engineering Research Council. I.F.A. was supported by FAPESP, Brazil. P.G. and J.R.P.M. were partially supported by FAPESP and CNPq, Brazil. A.M. was partially supported by CONACyT, Mexico.

M.A.K. was partially supported by the International Science Foundation.

REFERENCES

[1] Y. Hara, Phys. Rev. Lett. **12**, 378 (1964).

[2] L. K. Gershwin, *et al*, Phys. Rev. **188**, 2077 (1969).

[3] A. Manz, *et al*, Phys. Lett. **96B**, 217 (1980).

[4] M. Kobayashi, *et al*, Phys. Rev. Lett. **59**, 868 (1987).

[5] Particle Data Group, Phys. Rev D **50**, part I, 1173 (1994).

[6] G. Ang *et al*, Z. Phys **228**, 151 (1969).

[7] M. Bazin, *et al*, Phys. Rev. Lett. **14**, 154 (1965).

[8] N. P. Hessey *et al*, Z. Phys C **42**, 175 (1989).

[9] S. F. Biagi *et al*, Z. Phys. C **28**, 495 (1985).

[10] J. Mahon, Ph.D. Thesis, Univ. of São Paulo, (1993) (unpublished).

[11] T. Dubbs et al, Phys. Rev. Lett.,**72**, 808 (1994).

[12] I. Albuquerque *et al*, Phys. Rev. D **50**, 18 (1994).

[13] M. Foucher *et al.*, Phys. Rev. Lett., **68**, 3004 (1992).

[14] S. F. Biagi *et al*, Z. Phys C **35**, 143 (1987).

[15] S. Teige *et al*, Phys. Rev. Lett. **63**, 2717 (1989).

[16] C. James *et al*, Phys. Rev. Lett. **64**, 843 (1990).

[17] S. F. Biagi *et al*, Z. Phys. C **30**, 201 (1986).

[18] A. J. Noble *et al*, Phys. Rev. Lett **69**, 414 (1992).

[19] K. D. Larson *et al*, Phys. Rev. D **47**, 799-810 (1993).

[20] M. Bourquin *et al*, Nucl. Phys. **B241**, 1 (1984).

[21] M. Kawaguchi, K. Nishijima. Progr. Theor. Physics, **15**, 182 (1956)
C. Iso, M. Kawaguchi. Progr. Theor. Physics, **16**, 177 (1956)
R. E. Behrends, Phys. Rev **111**, 1691 (1958).

[22] P. Żenczykowski, Phys. Rev. D 40, 2290 (1989).

[23] B. Bassalleck, Nucl. Phys. **A547**, 299 (1992).

[24] Ya. I. Azimov in Proc. LNPI 22 Winter school of physics, 200 (1987).

[25] V. I. Zakharov, A. B. Kaidalov, Sov. J. Nucl. Phys. **5**, 259 (1967).

[26] G. Farrar, Phys.Rev. D **4**, 212 (1971).

[27] Ya. I. Kogan and M. A. Shifman, Yad. Fiz. **38**, 1045 (1983). [Sov. J. Nucl. Phys. **38**, 628 (1983)].

[28] J. Pati, Phys. Rev. **130**, 2097 (1963).

[29] R. Graham, S. Pakvasa, Phys. Rev. **140B**, 1144 (1965).

[30] A. Le Yaouanc *et al*, Nucl. Phys. **B149**, 321 (1979).

[31] M. D. Scadron and L. Thebaud, Phys. Rev. D **8**, 2190 (1973).

[32] M. D. Scadron and M. Visinescu, Phys Rev. D **28**, 1117 (1983).

[33] M. Gavela *et al*, Phys. Lett. B **101**, 417 (1981).

[34] F. Close and H. Rubinstein, Nucl. Physics. **B173**, 477 (1980).

[35] K. Rauh, Z. Phys. C **10**, 81 (1981).

[36] G. Nardulli, Nuovo Cimento A **100**, 485 (1988).

[37] P. Żenczykowski Phys. Rev. D 44 1485 (1991).

[38] F. J. Gilman and M. B. Wise, Phys Rev. D **19**, 976 (1979).

[39] Lo Chong-Huah, Phys. Rev. D **26**, 199 (1982).

[40] A. Kamal and R. Verma, Phys. Rev. D **26**, 190 (1982).

[41] R. Verma and A. Sharma, Phys. Rev. D **38**, 1443 (1988).

[42] T. Uppal and R. Verma, Z. Phys. C. **52**, 307 (1991).

[43] A. I. Vainshtein, V. I. Zakharov and M. A. Shifman, Sov. Phys. JETP Lett. **22**, 55 (1975)
M. A. Shifman, A. I. Vainstein and V. I. Zakharov, Nucl. Phys. **B120**, 316 (1977)
A. I. Vainshtein, V. I. Zakharov and M. A. Shifman, Sov. Phys. JETP **45**, 670 (1977)
F. J. Gilman and M. B. Wise, Phys. Lett. B **83**, 83 (1979)
B. Guberian and R. D. Peccei, Nucl. Phys. **B163**, 289 (1980).

[44] S. G. Kamath, Nucl. Phys. **B198**, 253 (1984)

[45] J. O. Eeg, Z. Phys. C **21**, 253 (1984).

[46] M. K. Gaillard, X. Q. Li, and S. Rudaz, Phys. Lett. **158B**, 158 (1985).

[47] V. M. Khatsymovsky, Sov. J. Nucl. Phys. **45**, 116 (1987)
Erratum, Sov. J. Nucl. Phys. **46**, 768 (1987).

[48] V. M. Khatsymovsky, Sov. J. Nucl. Phys. **46**, 496 (1987).

[49] I. I. Balitsky, V. M. Braun, A. V. Kolesnichenko, Sov. J. Nucl. Phys. **44**, 1028 (1986).

[50] The texts of these papers [47] and [49] give a large negative value for the asymmetry because they use an unconventional definition of the asymmetry.

[51] C. Goldman and C. O. Escobar, Phys. Rev. D **40**, 106 (1989).

[52] I. I. Balitsky, V. M. Braun, A. V. Kolesnichenko, Nucl. Phys. **B312**, 509 (1989).

[53] E. Jenkins, M. Luke, A. V. Manohar and M. J. Savage, Nucl. Phys. **B397**, 84 (1993).

[54] H. Neufeld, Nucl. Phys. **B402**, 166 (1992).

[55] S. Matinyan, Yad. Fiz. **2**, 151, (1965).

[56] M. Gourdin, Unitary Symmetry, 137, (North Holland, 1967).

[57] N. Vasanti Phys. Rev. D **13**, 1889 (1976).

[58] L. F. Li and Y. Liu, Phys. Lett. **195B**, 281 (1987).

[59] M. K. Gaillard, Phys. Lett. **211B**, 189 (1988).

[60] A. N. Kamal and Riazuddin, Phys. Rev. D **28**, 2317 (1983).

[61] A. Garcia and P. Kielanowski, The Beta Decay of Hyperons, Lecture Notes In Physics, Vol. 222, (Springer-Verlag, 1985).

[62] M. Roos, Phys. Lett. **246B**, 179, (1990).

[63] T. R. Cardello *et al*, Phys. Rev. D **32**, 1 (1985).

[64] Basel Convention Helv. Phys. Act. Suppl. VI, (1961).

[65] V. T. Grachev *et al*, in Proceedings of the Symposium on Particle Identification at High Luminosity Hadron Colliders, p. 415, Fermi National Accelerator Laboratory, Batavia, (1989).

[66] T. Ludlam *et al*, Nucl. Instr. and Meth. **180**, 413 (1991).

[67] C. W. Fabjan *et al*, Nucl. Instr. and Meth. **185**, 119 (1981).

[68] S. Y. Hsueh *et al*, Phys. Rev. D **38**, 2056, (1988).

[69] M. Foucher, Ph.D. Thesis, Yale University, (1992) (unpublished).

[70] T. Dubbs, Ph.D. Thesis, University of Iowa, (1993) (unpublished).

[71] F. James and M. Roos, CERN Program Library D506, (1988).

[72] R. Brun *et al*, GEANT3, DD/EE/84-1, CERN (1987).

FIGURES

FIG. 1. Diagrams for the processes contributing to hyperon radiative decays.

FIG. 2. Plan view of the E761 apparatus in the Fermilab Proton Center charged hyperon beamline.

FIG. 3. The photon spectrometer. The position of the electromagnetic shower in the steel converters is measured in PWC and TRD. The photon energy is measured in a photon calorimeter.

FIG. 4. Photon calorimeter (A) The front lead glass wall (B) The main lead glass array with BGO lining the hole (C) The rear lead glass array

FIG. 5. Results of charged-track analysis. Missing mass squared $M^2_{X^0}(GeV^2/c^4)$ assuming $\Sigma^+ \rightarrow p\, X^0$.

FIG. 6. Single-event display of TRD response for
(A) $\Sigma^+ \rightarrow p\, \gamma$ (TRD χ^2= 0.15, $M^2_{X^0} \;=\; 7.43 \times 10^{-4}\; GeV^2/c^4$)
(B) $\Sigma^+ \rightarrow p\, \pi^0$ (TRD χ^2= 50.0, $M^2_{X^0} \;=\; 0.0164\; GeV^2/c^4$)

FIG. 7. TRD χ^2 for signal region including $\Sigma^+ \rightarrow p\, \gamma$ (solid), $\Sigma^+ \rightarrow p\, \pi^0$ (dashed, normalized for equal sample size)

FIG. 8. (A) The missing mass squared distribution for all events with TRD $\chi^2 < 1.0$ (error bars) and TRD $\chi^2 > 4.0$ (background, solid curve) normalized to equal area in the interval [$0.0072 < M^2_{X^0} < 0.01$ GeV^2/c^4] where the distribution is dominated by hadronic decays. (B) Distribution of TRD χ^2 vs. $M^2_{X^0}$ for data used in the asymmetry calculation.

FIG. 9. Center of mass decay angles for PRE sample, assuming $\Sigma^+ \rightarrow p\, \pi^0$ (A) $\cos\theta_X$, (B) $\cos\theta_Y$, (C) $\cos\theta_Z$; where solid line is POS and dashed is NEG, asymmetry $\times \cos\theta$ as a function of decay angle for PRE sample (D) $\cos\theta_X$, (E) $\cos\theta_Y$, (F) $\cos\theta_Z$ where solid is after bias canceling and dashed is before.

FIG. 10. Center of mass decay angles for signal region assuming $\Sigma^+ \rightarrow p\,\gamma$ (A) $\cos\theta_X$, (B) $\cos\theta_Y$, (C) $\cos\theta_Z$; where solid line is POS and dashed is NEG, asymmetry × $\cos\theta$ as a function of decay angle for signal region (D) $\cos\theta_X$, (E) $\cos\theta_Y$, (F) $\cos\theta_Z$ where solid is after bias canceling and dashed is before.

FIG. 11. PRE sample (A) Θ_X of hyperon for (solid) POS, (dashed) NEG. The region selected to form (B) is shown. (B) $\cos\theta_X$, POS and NEG, $0.00325 < \Theta_X < 0.0035$, normalized to equal area.

FIG. 12. Missing neutral mass distributions (positive targeting angle) for (A) the PRE sample, where solid line is fit to all data described in Sec. V.B.1. and the dashed line indicates the linear background fit, (B) the Monte Carlo simulation, where the dashed line is the scaled fit from the data in (A).

FIG. 13. All POS $\Sigma^+ \rightarrow p\,\pi^0$ data, showing the fit (solid curve) of the resolution function to the data.

FIG. 14. PGAM sample missing neutral mass for (A) POS All TRD (B) NEG All TRD (C) POS TRD $\chi^2 < 10$ (D) NEG TRD $\chi^2 < 10$. Solid lines show fit with resolution function + linear and exponential background, dashed lines are background only.

FIG. 15. (A) TRD χ^2 for single photons from π^0 where the second photon was detected in rear lead glass. (B) Percentage of events included in TRD selection of a given χ^2 or less for (solid) single photons, (dashed) $\Sigma^+ \rightarrow p\,\pi^0$.

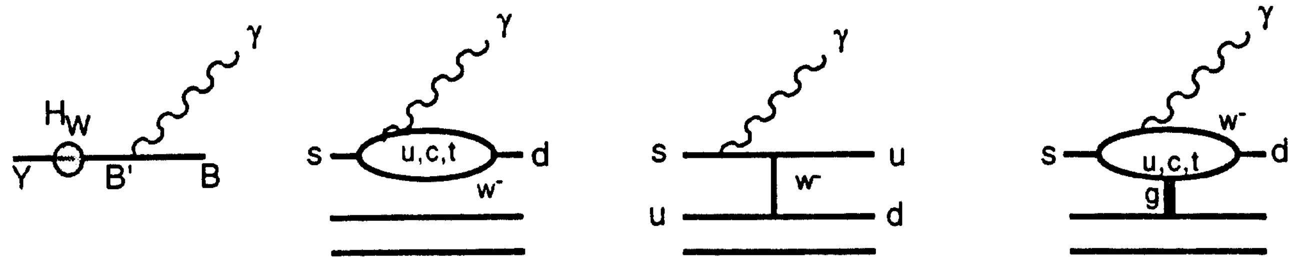

A. Pole model

B. Single-quark Transition

C. W Exchange

D. Penguin

DX 5032

FIG 1.

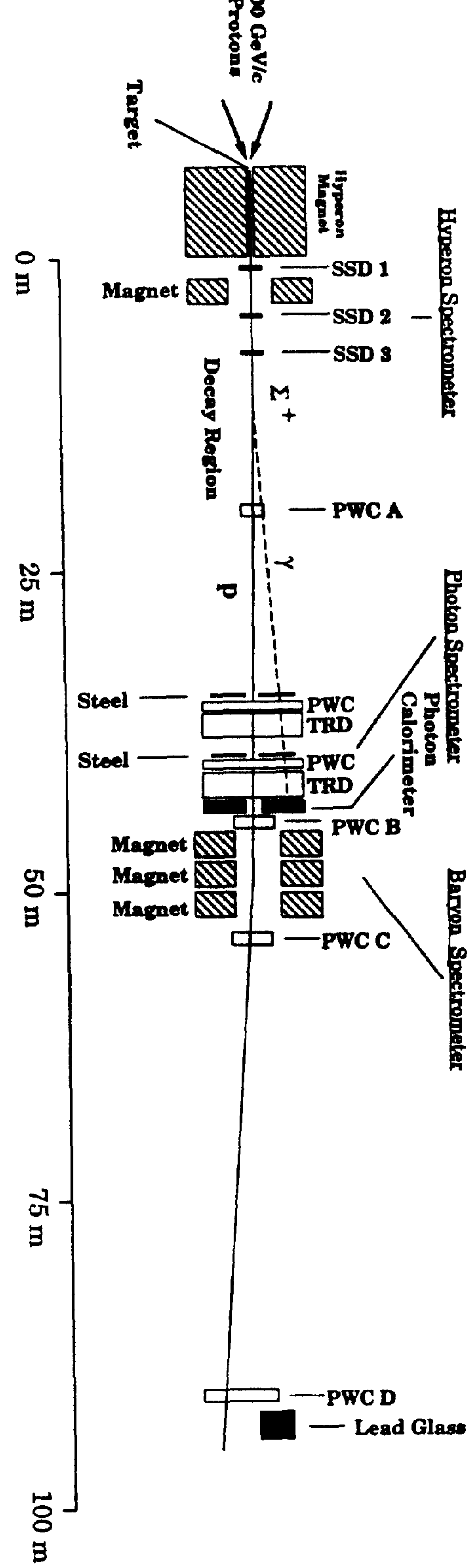

800 GeV/c Protons
Target
Hyperon Magnet
Hyperon Spectrometer
SSD 1
SSD 2
SSD 3
Magnet
Σ +
Decay Region
PWC A
γ
p
Photon Spectrometer
Photon Calorimeter
Steel
PWC
TRD
Steel
PWC
TRD
PWC B
Magnet
Magnet
Magnet
Baryon Spectrometer
PWC C
PWC D
Lead Glass
0 m
25 m
50 m
75 m
100 m

Dx5032
FIG 2

Photon spectrometer

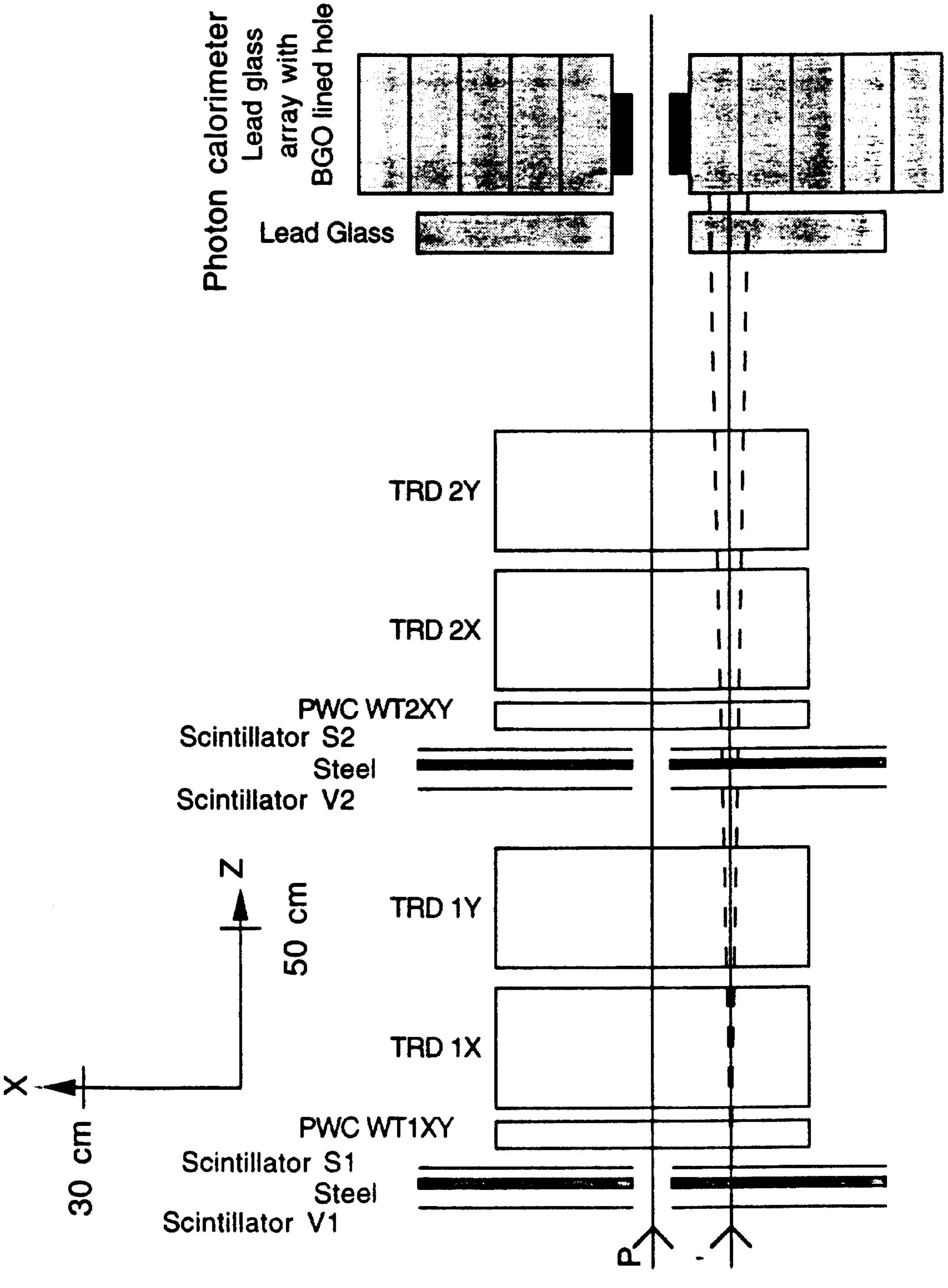

Dx5032
FIG 3

A. Lead glass front wall

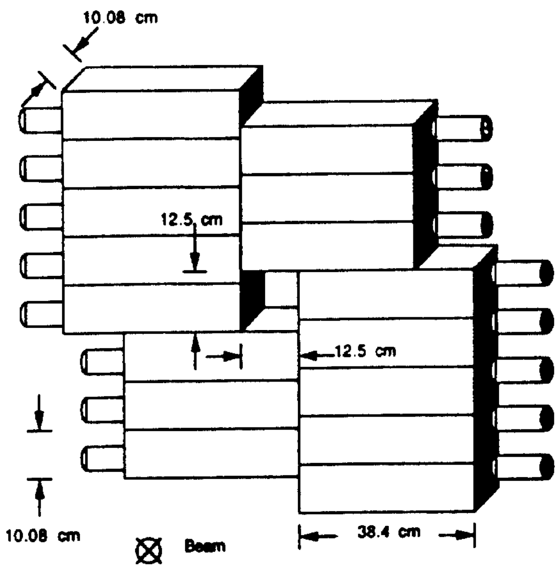

B. Lead glass main array

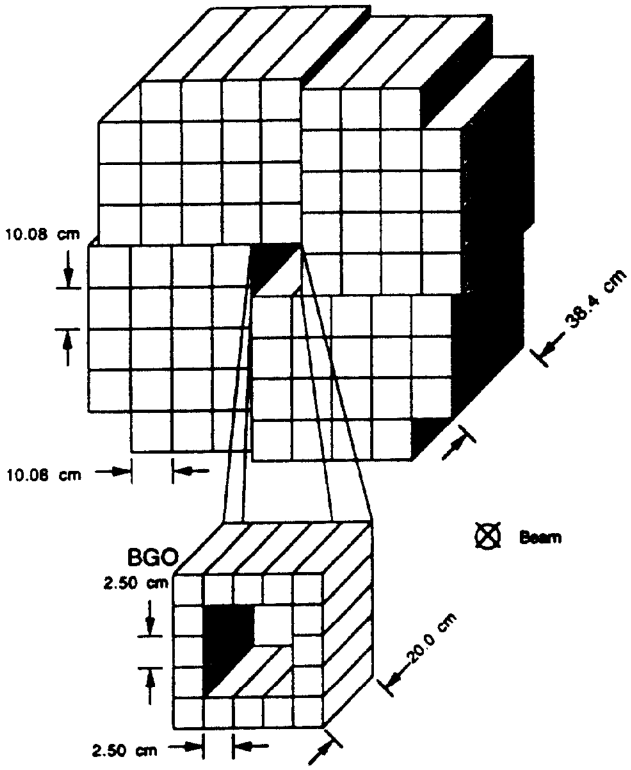

C. Rear lead glass

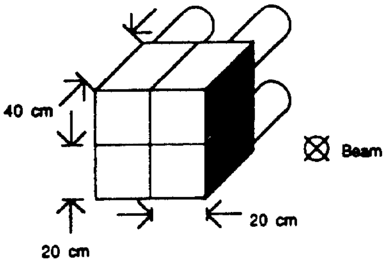

Dx5032
Fig 4

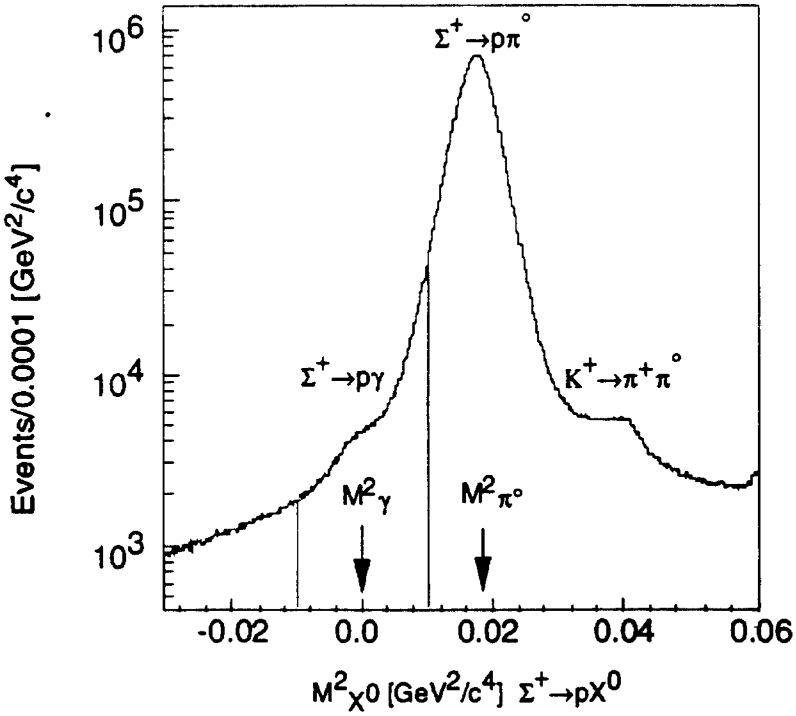

10^6
10^5
10^4
10^3
Events/0.0001 [GeV^2/c^4]
$\Sigma^+ \to p\pi^\circ$
$\Sigma^+ \to p\gamma$
$K^+ \to \pi^+\pi^\circ$
M^2_γ
$M^2_{\pi^\circ}$
-0.02
0.0
0.02
0.04
0.06
$M^2_{X^0}$ [GeV^2/c^4] $\Sigma^+ \to pX^0$

DxS032

FIG 5

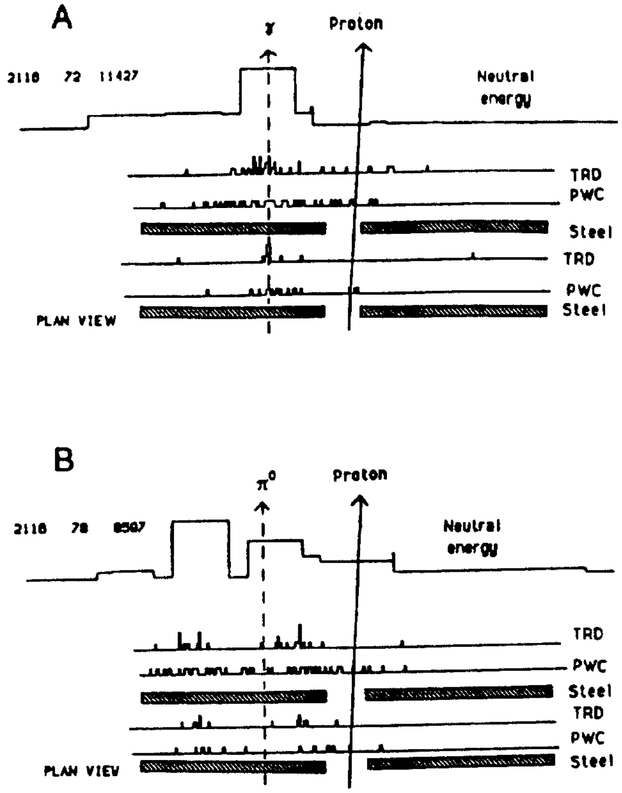
A
γ
Proton
2118 72 11427
Neutral energy
TRD
PWC
Steel
TRD
PWC
PLAN VIEW
Steel
B
π^0
Proton
2118 78 8597
Neutral energy
TRD
PWC
Steel
TRD
PWC
PLAN VIEW
Steel

DX5032

FIG 6

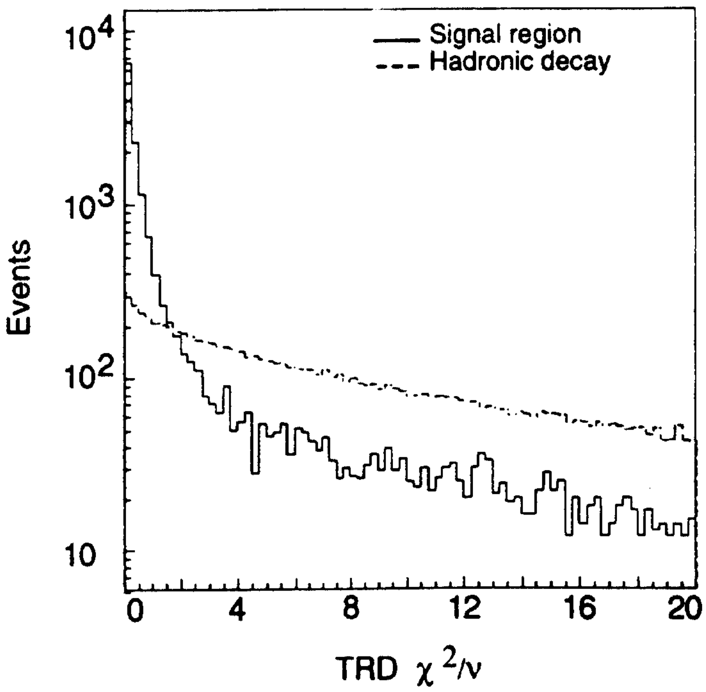
Signal region
Hadronic decay
Events
10^4
10^3
10^2
10
0
4
8
12
16
20
TRD χ²/ν

Dx5032

FIG 7

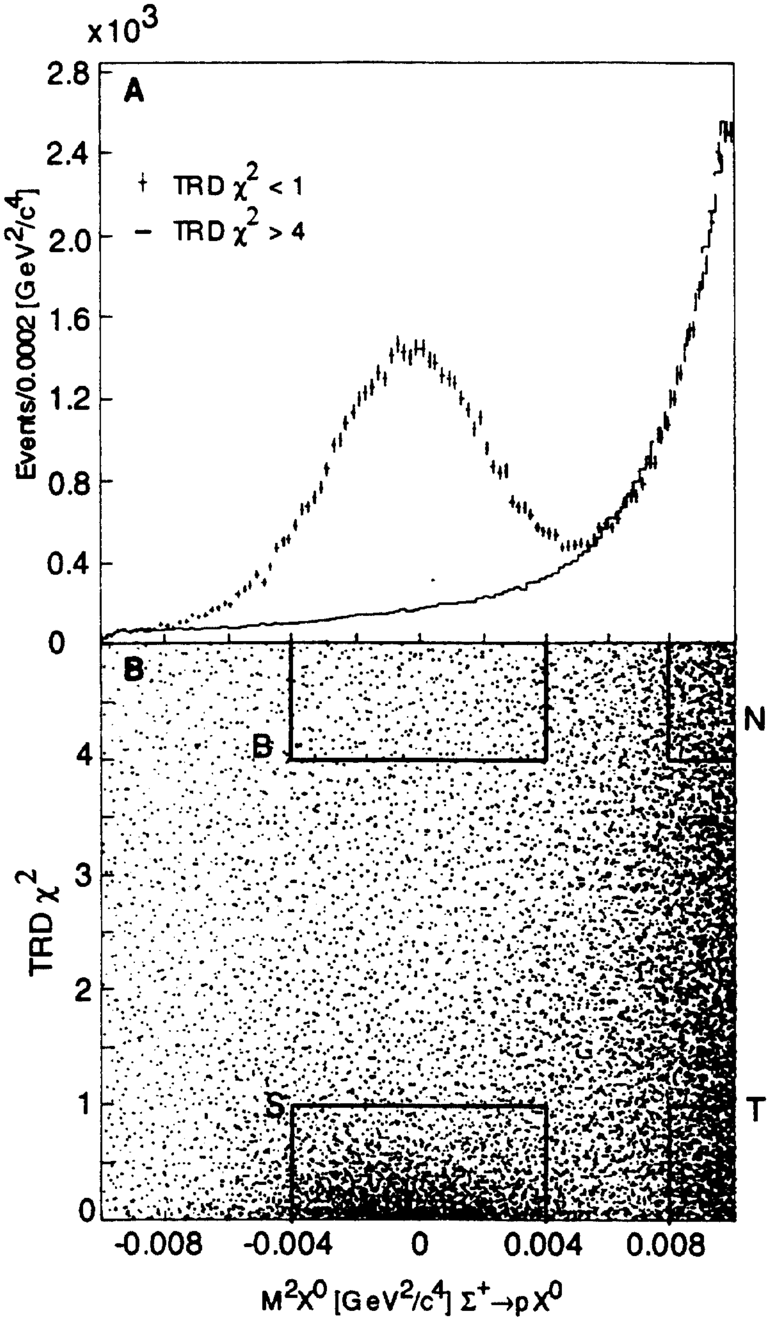
x10^3
A
TRD χ^2 < 1
TRD χ^2 > 4
Events/0.0002 [GeV^2/c^4]
2.8
2.4
2.0
1.6
1.2
0.8
0.4
0
B
B
N
S
T
TRD χ^2
4
3
2
1
0
-0.008
-0.004
0
0.004
0.008
M^{2}X^0 [GeV^2/c^4] $\Sigma^+ \to pX^0$

DX 5032
FIG 8

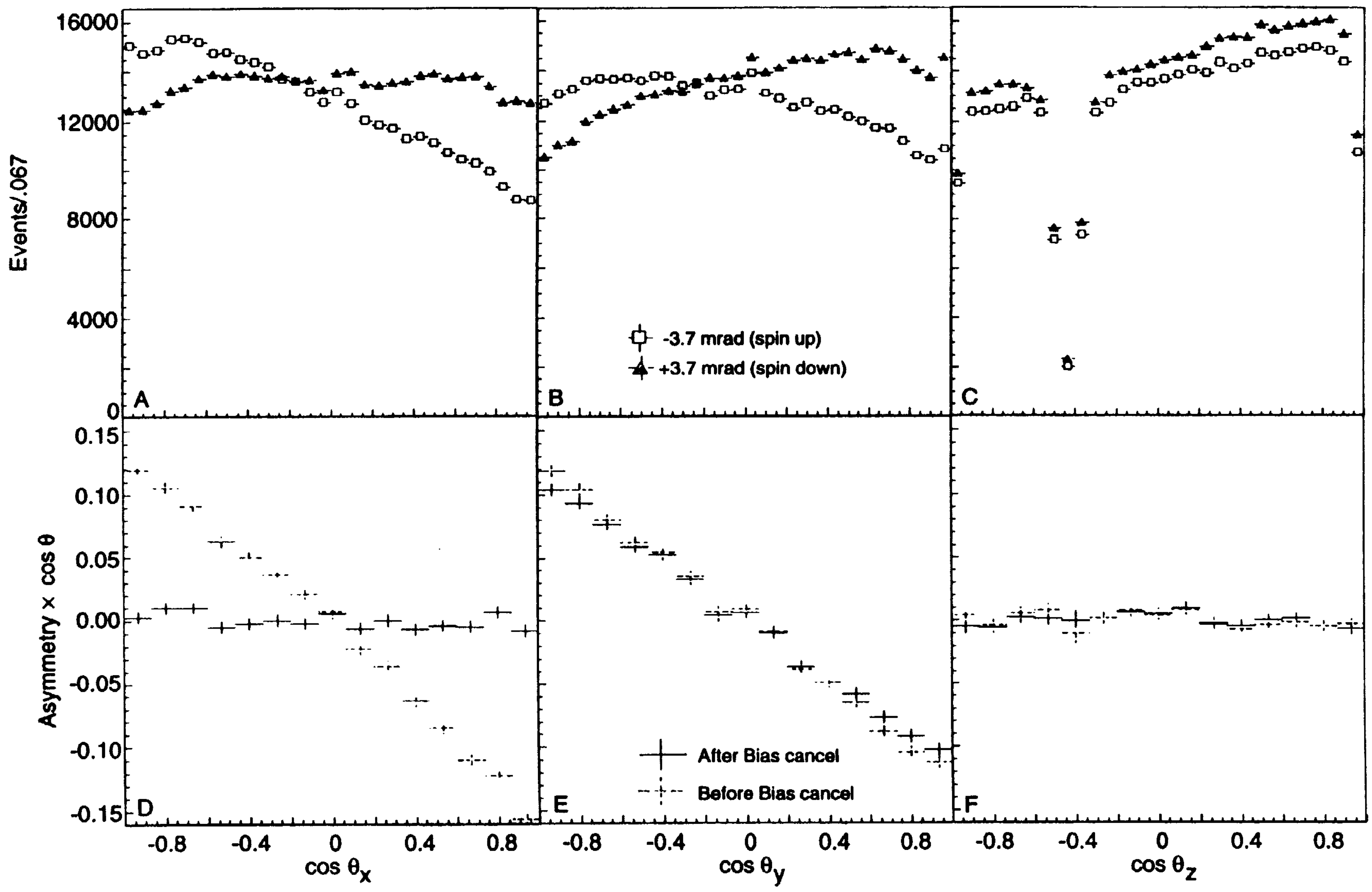
Events/.067
16000
12000
8000
4000
0
A
B
C
-3.7 mrad (spin up)
+3.7 mrad (spin down)
Asymmetry × cos θ
0.15
0.10
0.05
0.00
-0.05
-0.10
-0.15
D
E
F
After Bias cancel
Before Bias cancel
-0.8
-0.4
0
0.4
0.8
cos θx
cos θy
cos θz

Dx 5032

FIG 9

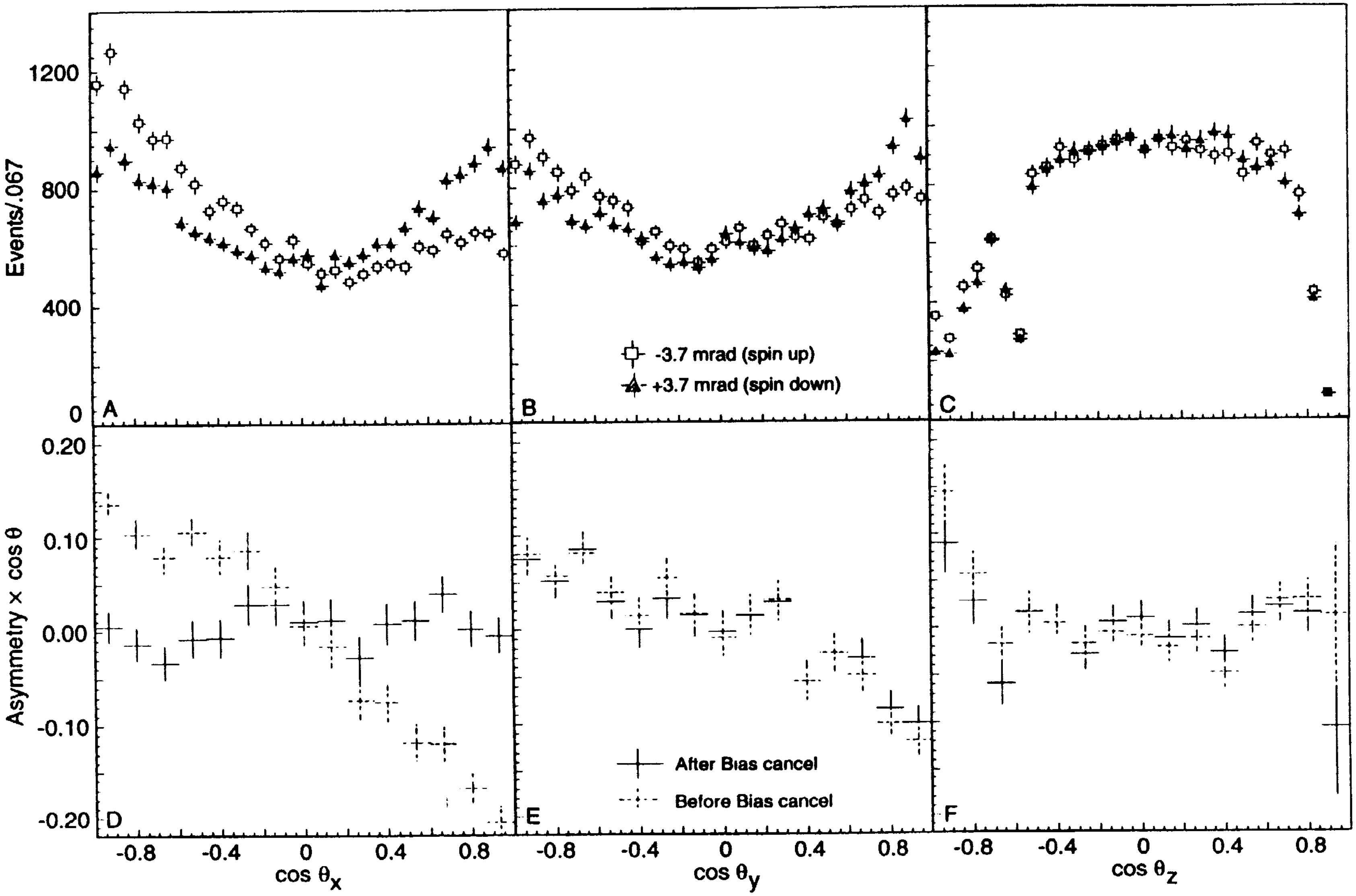

DxS032

FIG 17

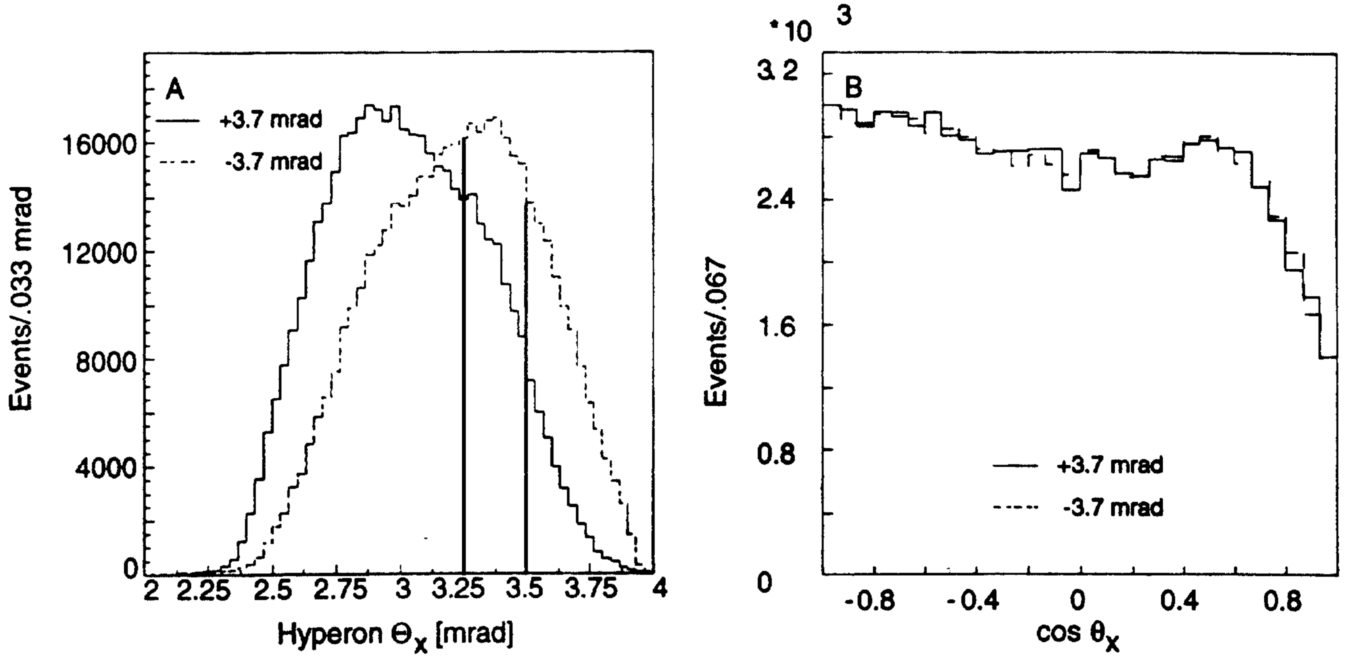

Dx5032

FIG 11

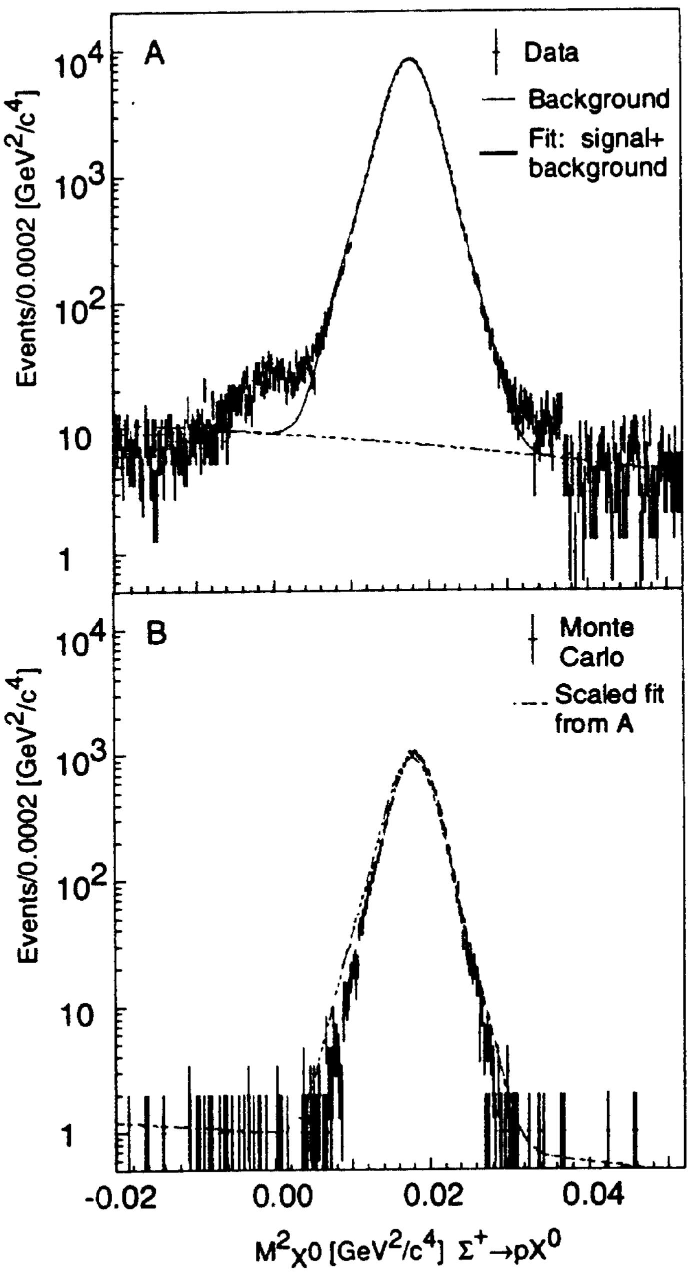

Dx 5032
FIG 12

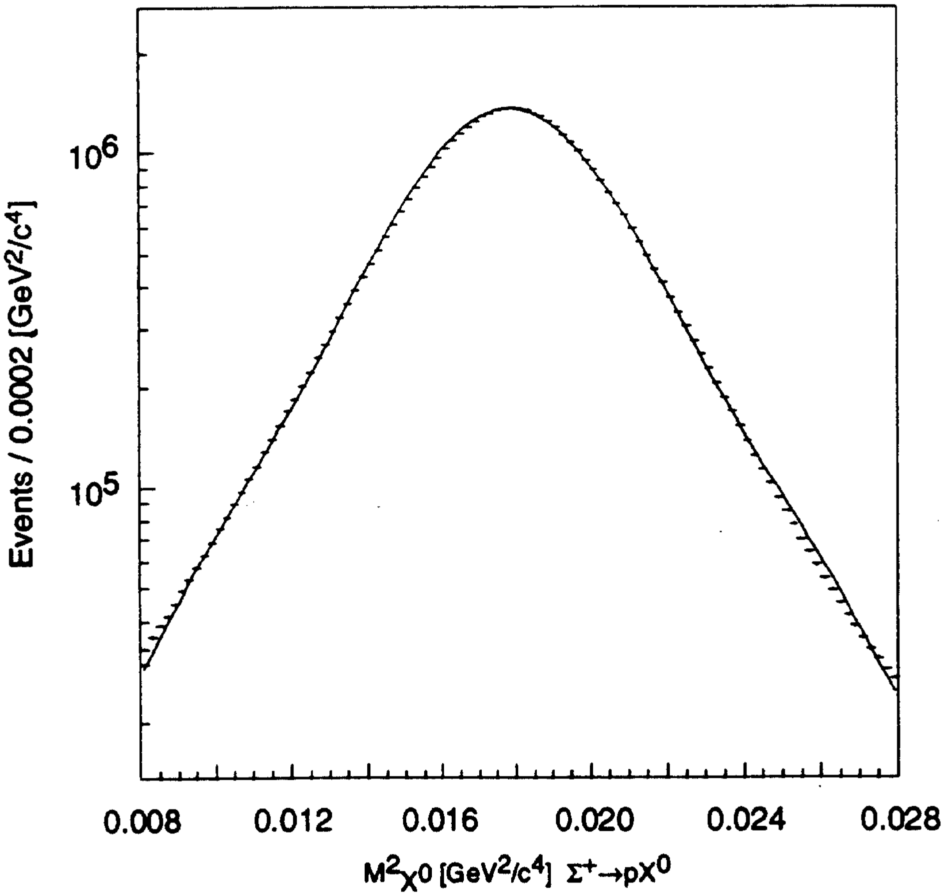

Dx5032

FIG 13

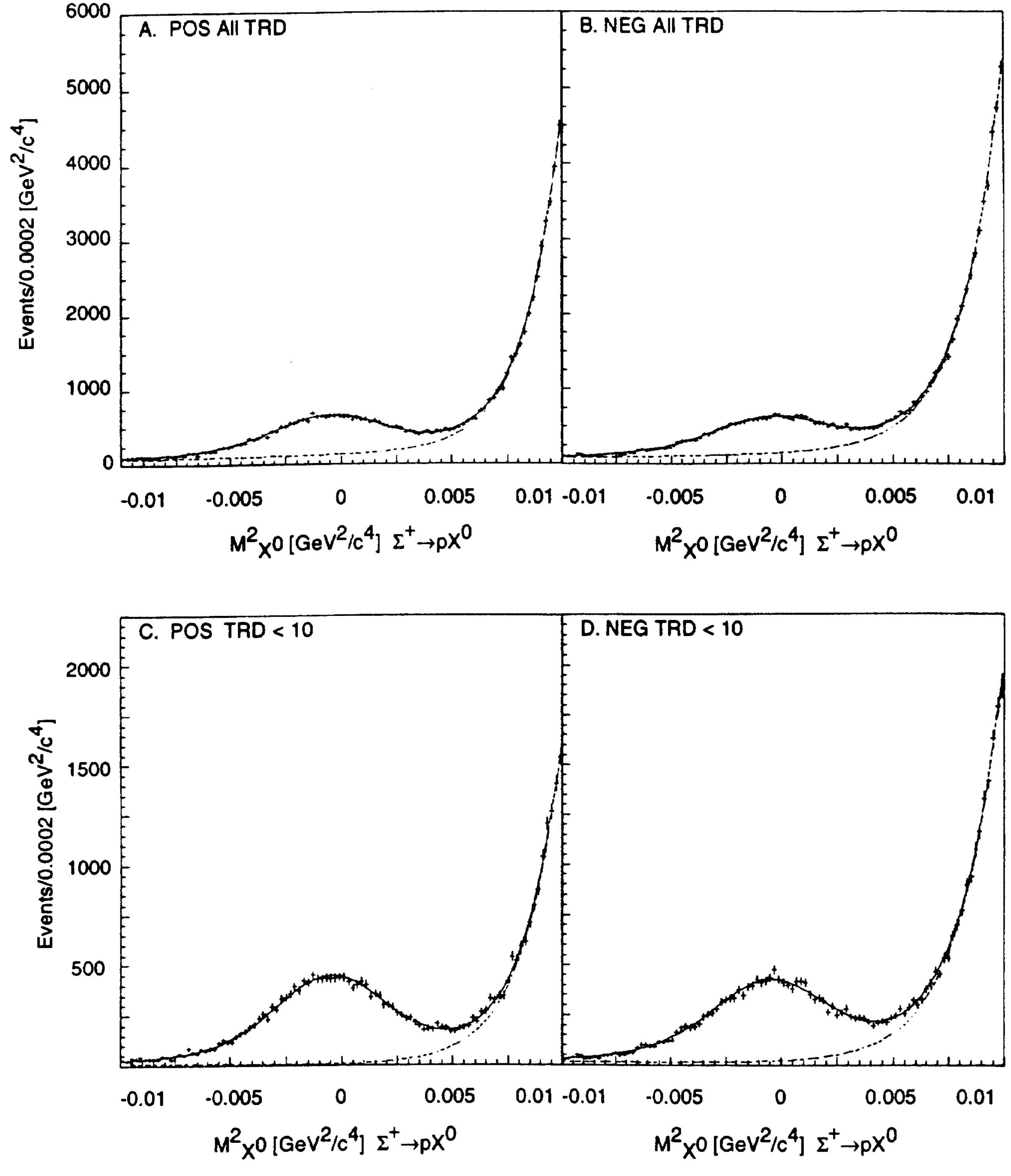

Dx5032
FIG 14

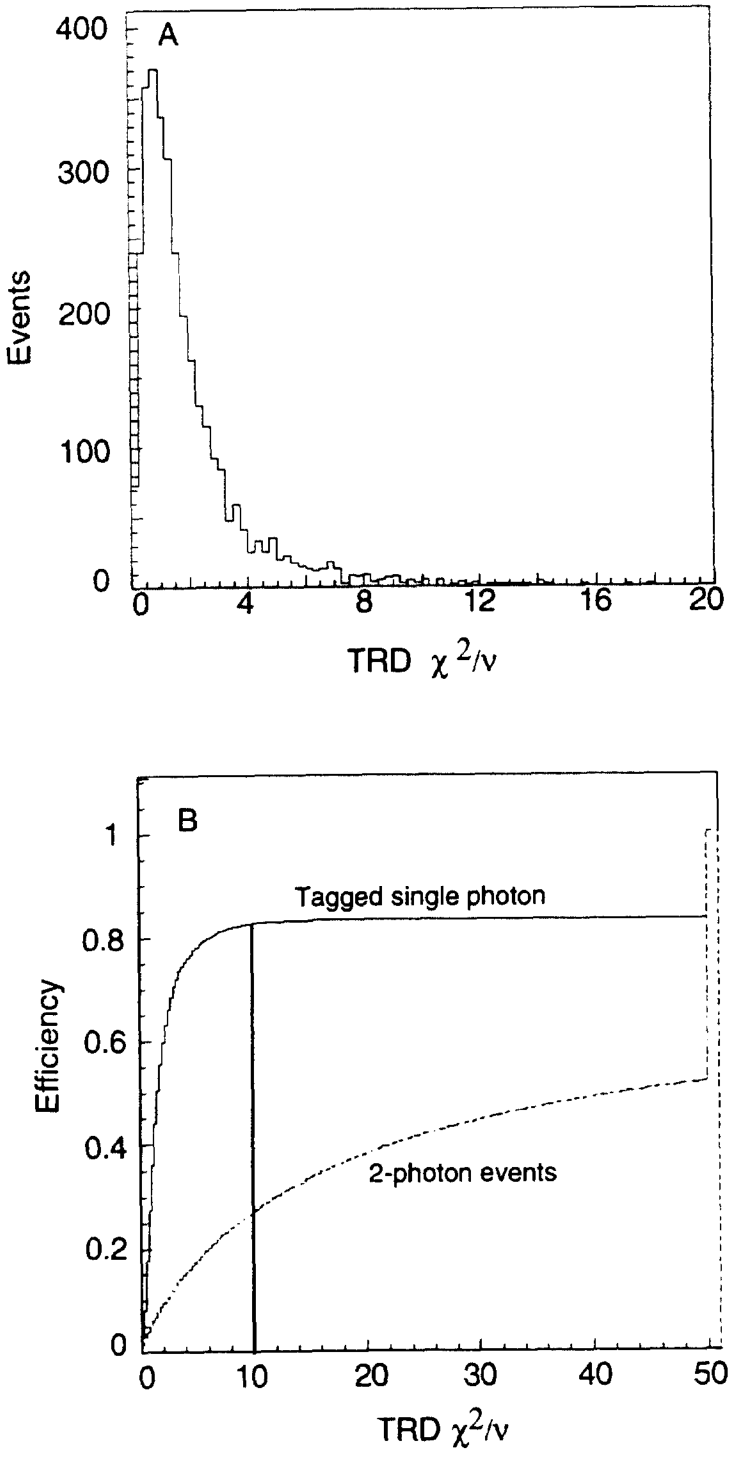

DxS032

FIG 15